Coarse-Grained Molecular Simulation of the Hierarchical Self-Assembly of π-Conjugated Optoelectronic Peptides

Rachael A. Mansbach[†] and Andrew L. Ferguson[*,‡,¶]

Department of Physics, University of Illinois at Urbana-Champaign, 1110 W Green St, Urbana, IL 61801, USA, and Department of Materials Science and Engineering, University of Illinois at Urbana-Champaign, 1304 W Green St, Urbana, IL 61801, USA

E-mail: alf@illinois.edu

Phone: (217) 300-2354. Fax: (217) 333-2736

[*]To whom correspondence should be addressed

[†]Department of Physics, University of Illinois at Urbana-Champaign, 1110 W Green St, Urbana, IL 61801, USA

[‡]Department of Materials Science and Engineering, University of Illinois at Urbana-Champaign, 1304 W Green St, Urbana, IL 61801, USA

[¶]Department of Chemical and Biomolecular Engineering, University of Illinois at Urbana-Champaign, Urbana, IL 61801, USA

Abstract

Self-assembled aggregates of peptides containing aromatic groups possess optoelectronic properties that make them attractive targets for the fabrication of biocompatible electronics. Molecular-level understanding of how the microscopic peptide chemistry influences the properties of the aggregates is vital for rational peptide design. We construct a coarse-grained model of Asp-Phe-Ala-Gly-OPV3-Gly-Ala-Phe-Asp (DFAG-OPV3-GAFD) peptides containing OPV3 (distyrylbenzene) π-conjugated cores explicitly parameterized against all-atom calculations and perform molecular dynamics simulations of the self-assembly of hundreds of molecules over hundreds of nanoseconds. We observe a hierarchical assembly mechanism wherein $\sim$2-8 peptides assemble into stacks with aligned aromatic cores that subsequently form elliptical aggregates and ultimately a branched network with a fractal dimensionality of $\sim$1.5. The assembly dynamics are well described by a Smoluchowski coagulation process for which we extract rate constants from the molecular simulations to both furnish insight into the microscopic assembly kinetics and extrapolate our aggregation predictions to time and length scales beyond the reach of molecular simulation. This study presents new molecular-level understanding of the morphology and dynamics of the spontaneous self-assembly of DFAG-OPV3-GAFD peptides and establishes a systematic protocol to develop coarse-grained models of optoelectronic peptides for the exploration and design of π-conjugated peptides with tunable optoelectronic properties.

1. INTRODUCTION

As the understanding of biological molecules and techniques to synthesize new materials continues to improve, there is growing interest in "designer" nanomaterials: organic materials that can be tuned at a microscopic level to produce desirable macroscopic properties. Proteins and polymers that display triggerable self-assembly into supramolecular aggregates have proven to be valuable components in the fabrication of such nanomaterials[1] with a wide range of potential applications including drug delivery, tissue regeneration[2–4], and as biomineralization scaffolds for tooth and bone growth[5,6]. Furthermore, "smart" self-assembling peptide-based materials have found multifarious applications in biosensing due to their ability to respond to diverse stimuli including pH, temperature, metal ion concentration, enzymatic activity, and light bombardment[7]. In other cases, such external stimuli have been used to tune the properties of the resultant aggregates for specific applications in materials design[8], biomedical diagnostics[9], and bioelectronics[10].

Self-assembling π-conjugated peptides are easily synthesizable, water soluble, and biocompatible. Their optoelectronic functionality – due to overlap and delocalization of the π orbitals within the supramolecular aggregates[11] – makes them well suited for bioelectronic applications such as organic field-effect transistors, light-emitting diodes, and photovoltaic cells[12–16]. They also display promising tunability, with assembly behavior and emergent photophysical and electronic properties of the aggregates controllable by manipulation of the chemistry of the conjugated cores and side chain moieties and the prevailing environmental conditions[13]. Several experimental and computational studies have been performed on π-conjugated peptide systems containing oligophenylenevinylene (OPV) cores. It has been demonstrated that these systems can undergo β-sheet-like assembly into one-dimensional nanostructures whose optoelectronic properties can be tuned from excimeric-like to excitonic-like by changing the chemistry and symmetry of the molecules[16–19]. In this paper, we focus on the symmetric Asp-Phe-Ala-Gly-OPV3-Gly-Ala-Phe-Asp (DFAG-OPV3-

GAFD) oligopeptide containing an OPV3 (distyrylbenzene) π-conjugated core in which the N-to-C directionality of the peptide wings proceeds away from the OPV3 core such that the molecule possesses two C-termini (Fig. 1a)[17,18]. At high pH, these peptides exist as dispersed monomers or small oligomers with large-scale assembly prohibited by electrostatic repulsion between the doubly negatively charged aspartic acid termini[20]. At low pH, protonation of the termini eliminates the electrostatic repulsion and triggers assembly into long β-sheet-like aggregates mediated by hydrogen bonding, π-π stacking, and dispersion interactions between the peptide cores and side chains[15–17,19,20], producing structures similar to amyloid fibrils[21].

Previous theoretical and computational work on DFAG-OPV3-GAFD assembly has included simulations of dimer aggregation and dimerization potentials of mean force[16], simulation and characterization of the morphology of preformed one-dimensional nanostructures of tens of monomers[18], and the characterization of the early stages of assembly up to tens of nanoseconds using implicit solvent molecular dynamics simulations and a Markov state model[20]. These works shed valuable light on both the kinetics of early-stage assembly and the effects of chemistry on the morphology of preformed aggregates. No studies to date have directly simulated the assembly of aggregates containing more than $\sim$10 oligopeptides, and it is of interest to probe longer time and length scales to determine the morphology and dynamics of assembly beyond these small-scale and early-stage events.

In this work, we construct a coarse-grained molecular model explicitly parameterized against all-atom calculations that enables us to perform molecular dynamics simulations of the assembly of hundreds of monomers over hundreds of nanoseconds. The structure of this paper is as follows. In Section 2, we describe our development of a coarse-grained DFAG-OPV3-GAFD model from all-atom calculations and our use of this model to perform coarse-grained molecular dynamics simulations. In Section 3, we report the results of our coarse-grained simulations, characterize the morphology of the self-assembly pathway, and extract microscopic rate constants to parameterize a Smoluchowksi coagulation model of non-equilibrium dynamics of peptide assembly. In Section 4, we present our conclusions and

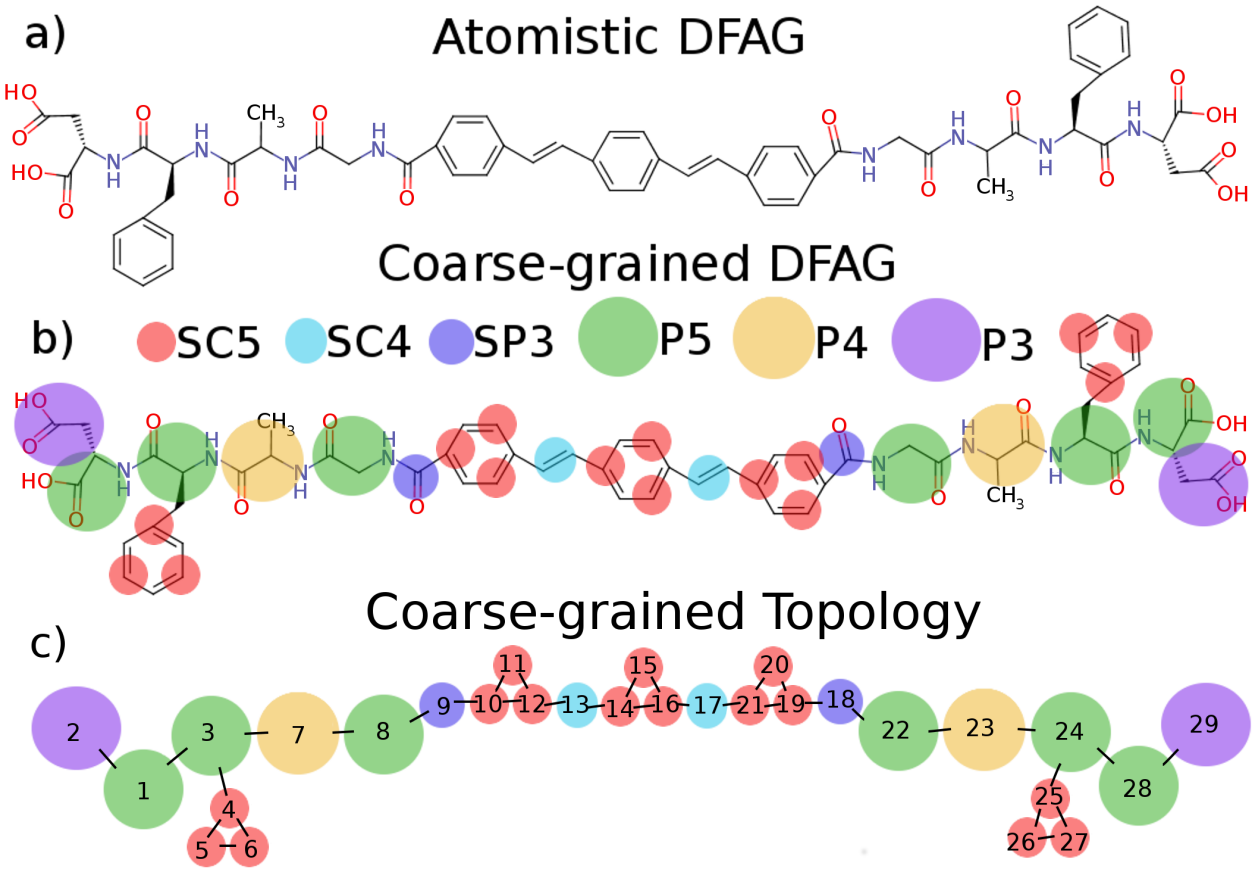

Figure 1: Atomistic and coarse-grained representations of the Asp-Phe-Ala-Gly-OPV3-Gly-Ala-Phe-Asp (DFAG-OPV3-GAFD) π-conjugated oligopeptide. These molecules are symmetric in the sense that each of the peptidic wings possess N-to-C directionality proceeding away from the π-conjugated core such that there are two C-termini[17,18]. (a) Chemical structure of DFAG-OPV3-GAFD, produced using Marvin 15.12.7.0 (ChemAxon, 2015) (http://www.chemaxon.com). Under high pH conditions (pH $\gtrsim$ 10), the distal aspartic acid residues are doubly negatively charged, prohibiting large-scale assembly due to electrostatic repulsion; at low pH (pH $\lesssim$ 2), protonation of the terminal residues leads to large-scale aggregation of the electrically neutral molecules[18]. (b) Mapping of the DFAG-OPV3-GAFD oligopeptide from an all atom representation to a coarse-grained representation under the Martini model[22,23]. Colored circles represent different coarse-grained beads formed by lumping of atoms. Detailed descriptions of the Martini beads may be found in Monticelli et al.[22]. (c) Coarse-grained topology of the DFAG-OPV3-GAFD oligopeptide with bonds and bead numbering scheme implemented in the coarse-grained adaptation of the Martini force field that we explicitly reparameterize against all-atom calculations. Full details of the force field are provided in the Supporting Information.

outlook for future work.

2. THEORETICAL METHODS

In this section, we report the development of a coarse-grained model explicitly parameterized against all-atom calculations, describe the simulation of hundreds of coarse-grained monomers over hundreds of nanoseconds at different concentrations, and define structural measures used to characterize cluster morphology.

2.1 Development of a coarse-grained model through atomistic and coarse-grained molecular dynamics simulations

Molecular dynamics simulations provide a means to link the chemical details of self-assembling peptides to the emergent structural and functional properties of self-assembled aggregates, providing a route to molecular-level mechanistic understanding and rational materials design[1]. All-atom simulations of hundreds of thousands of atoms over microsecond time scales are computationally challenging. Coarse-grained or multiphysics models reduce the number of degrees of freedom, providing the efficiency gains necessary to access the time and length scales required to robustly observe assembly[24–26]. Coarse-grained molecular dynamics simulations in which groups of atoms are lumped together into single beads have been employed to elucidate the structural and functional properties of large systems, including proteins[27,28], DNA[29], lipids and lipid membranes[24], and even bacterial flagella[30].

In this work, we develop a coarse-grained potential based on the Martini potential[22,23], which is a popular coarse-grained model[31] of proteins[23,32], lipids[33], and carbohydrates[34] that has been profitably employed to study peptide self-assembly[35,36]. The Martini force field is computationally efficient, transferable, and explicitly distinguishes between the 20 natural amino acid side chains[22,37] providing a good balance between computational efficiency and chemical realism that permits us to explicitly link oligopeptide sequence to emergent assembly behavior. As we describe below, we construct coarse-grained Martini models for the DFAG-OPV3-GAFD oligopeptide and then recalibrate the Martini parameters against

all-atom simulation data to develop a coarse-grained force field offering ∼25× speedups over all-atom calculations. The approach we present offers a systematic means to develop efficient and accurate bespoke coarse-grained potentials explicitly incorporating atomistic information.

2.1.1. All-atom molecular dynamics simulations for coarse-grained model parameterization

We employed the Gromacs 4.6 simulation suite[38] to perform all-atom molecular dynamics simulations of a single DFAG-OPV3-GAFD molecule solvated in water. Initial peptide configurations were prepared using the GlycoBioChem PRODRG2 server[39]. Peptides were prepared with protonated Asp termini corresponding to the electrically neutral, low-pH form of these molecules that have been experimentally demonstrated to exhibit triggered self-assembly under acidic conditions[17]. We modeled water explicitly using the TIP3P model[40], and treated the peptides using the CHARMM27 force field[41] supplemented with bonded parameters required to model the OPV3 core as described in Thurston et al.[20]. Simulations were conducted in the NPT ensemble at 298 K and 1 bar using a Nosé-Hoover thermostat[42] and Parrinello-Rahman barostat[43]. Three-dimensional periodic boundary conditions were employed. Initial atom velocities were randomly assigned from a Maxwell-Boltzmann distribution at 298 K and high energy overlaps in initial configurations were eliminated by performing steepest descent energy minimization to remove forces exceeding 500 kJ/mol-nm. The equations of motion were numerically integrated using a leap-frog algorithm[44] with a 2 fs time step, and bond lengths were fixed using the LINCS algorithm to improve efficiency[45]. Electrostatic interactions were treated using Particle Mesh Ewald (PME) with a real-space cutoff of 1.2 nm and a 0.12 nm Fourier grid spacing[46]. Lennard-Jones interactions were shifted smoothly to zero at 1.2 nm, and Lorentz-Berthelot combining rules were used to determine interaction parameters between unlike atoms[47]. Calculations were performed on 40 × 2.2 GHz Intel Xeon E5-2430 CPU cores, achieving execution speeds of ∼30 ns/day.

Isolated molecules. A single DFAG-OPV3-GAFD molecule was placed in a $7 \times 7 \times 7$ nm^3 box, which was sufficiently large to preclude direct interactions of the peptide with its own periodic image in its fully-extended state. The peptide was then solvated to a density of 0.988 g/cm^3 with TIP3P water[40] and an equilibration run of 10 ps performed, after which time the density, energy, temperature, and pressure had attained stable values. A production run of 340 ns was conducted to comprehensively sample the intramolecular degrees of freedom.

Monomer potential of mean force. The end-to-end potentials of mean force (PMF) quantifying the free energy of a monomer as a function of the distance between its terminal carbon atoms were computed using umbrella sampling in the end-to-end distance[48]. The oligopeptide termini were restrained at intermolecular separations between 0.0 nm and 4.0 nm at intervals of 0.1-0.2 nm to assure good overlap of neighboring umbrella window histograms. A harmonic restraining potential of 1000 kJ/mol-nm^2 was employed in each window, and the system allowed to relax for 100 ps prior to a 10 ns production run. End-to-end distances were recorded and the PMF computed by self-consistent solution of the weighted histogram analysis method (WHAM) equations[49] to a tolerance of 10^{-6} in the estimated probability distribution, and uncertainties estimated by block averaging.

Dimerization potential of mean force. Dimerization PMFs quantifying the free energy as a function of the center of mass separation between a pair of monomers were computed in umbrella sampling calculations in which the monomer pair was restrained at separations between 0.0 nm and 5.0 nm at intervals of 0.1-0.2 nm using a harmonic potential with a force constant of 1000 kJ/mol-nm^2. The largest separation considered was sufficient to observe a plateau in the PMF corresponding to a regime in which the monomers are effectively non-interacting. The dimerization PMF was computed by solving the WHAM equations[49] to a tolerance of 10^{-6} in the estimated probability distribution, and uncertainties estimated by block averaging.

2.1.2. Coarse-grained mapping and force field parameterization

Coarse-grained models of the DFAG-OPV3-GAFD molecule were prepared in the low pH state (pH $\lesssim$ 1) in which the aspartic acid residues are fully protonated and the molecule is electrically neutral, and the high pH state (pH $\gtrsim$ 10) in which the aspartic acids are fully deprotonated and the molecule carries a net charge of (-4)[18,20]. We first describe the construction of the protonated (low pH) coarse-grained model, and then the modifications made for the deprotonated (high pH) model. Construction of the coarse-grained model from all-atom simulation data proceeds in three stages: (i) mapping from all-atom to coarse-grained topology, (ii) definition of non-bonded (intermolecular) interactions between coarse-grained beads, and (iii) definition of bonded (intramolecular) interactions between the beads. We now describe each step in turn.

Coarse-grained mapping. A coarse-grained representation of the electrically neutral (low-pH) DFAG-OPV3-GAFD was constructed from the all-atom structure using the Martini model in which approximately four heavy atoms are mapped to a single bead (Fig. 1b)[22,23]. An initial molecular topology was built using the martinize.py script available from the Martini website (http://www.cgmartini.nl)[23], which was subsequently modified to treat the aromatic rings as described in the Martini force field[50] and the peptide-core linker regions following the guidelines on the Martini website (http://www.cgmartini.nl/index.php/faq/topologies) (Fig. 1c).

Non-bonded interactions. The non-bonded interactions were treated using the Martini force field (version 2.2)[23] and the non-polarizable Martini water model[51].

Bonded interactions. Bonded parameters for the coarse-grained bond stretching, angle bending, and proper and improper dihedrals were extracted from our 340 ns all-atom simulation trajectory using Boltzmann inversion to infer an effective coarse-grained potential from the all-atom intramolecular distributions[26,26,52]. By explicitly calculating the bonded potentials in this manner we developed a bespoke coarse-grained model that exhibited improved agreement with the all-atom calculations compared to the standard Martini parameters (see

Supporting Information). A deficiency of coarse-grained models is that they frequently do not adequately reproduce the intramolecular secondary structure of the all-atom model (cf. the monomer collapse PMF of the unmodified Martini model in Fig. 2a). In addition to reparameterizing each bonded Martini interaction, we follow Seo et al.[36] and apply proper dihedrals to every group of four consecutive beads in the backbone to enforce the backbone conformations observed in the all-atom calculations. The specific beads participating in these additional proper dihedrals and the parameters of the dihedral potential (cf. Eqn. 1) are listed in Tables S5-S8 in the Supporting Information.

To compute the effective coarse-grained potentials, we first located the hypothetical coarse-grained beads within the all-atom simulation trajectory as the centers of mass of the atoms mapped to each of the corresponding coarse-grained beads. We then compiled histograms of the distribution functions for each coarse-grained bonded interaction over the course of the all-atom trajectory under this coarse-grained mapping and extracted tabulated effective coarse-grained bonded potentials from these histograms. Both procedures were performed by using the Direct Boltzmann Inversion module in the Coarse-graining Toolkit of the Versatile Object-oriented Toolkit for Coarse-graining Applications software package (VOTCA-CSG)[53]. In implementing these effective potentials in Gromacs, the bond stretching and angle bending potentials were represented directly as tabulated potentials produced by VOTCA, whereas the periodic proper dihedrals were represented in the form,

$$V_d(\phi) = \sum_{n=1}^{4} C_n \left[1 + \cos(n\phi)\right] + \sum_{n=0}^{4} S_n \left[1 + \cos\left(n\phi - \frac{\pi}{2}\right)\right] \tag{1}$$

by constructing least squares fits in $\{C_n\}_{n=1}^{4}$ and $\{S_n\}_{n=0}^{4}$ to the tabulated potential using Matlab[54]. For convenience of representation in Gromacs, the improper dihedrals were represented using the same functional form as the propers. The distribution functions for bond lengths within the rigid aromatic rings were observed to be extremely narrow, so – similar to the rigid coarse-grained model of benzene due to Marrink et al.[51] – we elected to treat aro-

matic bond lengths as hard constraints enforced by the LINCS algorithm[45]. The symmetric DFAG-OPV3-GAFD molecule contains several chemically identical bonded interactions, and we improved the sampling in our inversion procedure by averaging the calculated effective potentials over all equivalent bonded interactions.

Protonated (low pH) and deprotonated (high pH) models. The low pH state in which the aspartic acid residues are fully protonated requires two modifications to construct a high pH model containing deprotonated aspartic acid residues. First, the aspartic acid beads were converted from P3 and P5 semi-attractive beads to negatively charged Qa beads, corresponding to the Martini treatment of the change in the Asp protonation state[22]. Secondly, the water was treated by the Martini polarizable water model, which, despite its higher computational cost, is a more realistic model for systems containing charged particles where polarization effects are anticipated to be important[55].

2.1.3. Coarse-grained molecular dynamics simulations for model parameterization

Isolated molecules. In order to assess the quality of the original Martini and reparameterized coarse-grained models, we performed coarse-grained molecular dynamics simulations of a single monomer in solution. Calculations were conducted in the Gromacs 4.6 simulation suite[56]. A single DFAG-OPV3-GAFD peptide was placed in a $7 \times 7 \times 7$ nm^3 box, which was sufficiently large to preclude direct interactions of the peptide with its own periodic image even in its fully-extended state. The peptide was then solvated to a density of 0.988 g/cm^3 with Martini non-polarizable[51] or Martini polarizable[55] water, depending on which model was being tested. Simulations were conducted in the NPT ensemble at 298 K and 1 bar, employing a velocity rescaling thermostat[57], a Parrinello-Rahman barostat[43], and three-dimensional periodic boundary conditions. Initial velocities were randomly assigned from a Maxwell-Boltzmann distribution at 298 K, and high energy overlaps in the initial configurations eliminated by performing steepest descent energy minimization to remove

forces exceeding 1000 kJ/mol-nm. Equations of motion were numerically integrated using a leap-frog algorithm[44] with a model-dependent time step, and constrained bond lengths fixed using the LINCS algorithm[45]. Lennard-Jones interactions were shifted smoothly to zero at 1.1 nm. Electrostatic interactions were treated using reaction field electrostatics and a relative electrostatic screening of 2.5 for polarizable water and 15 for non-polarizable water. An equilibration run of 10 ps was performed, after which time the density, energy, temperature, and pressure had attained stable values. Following equilibration, a production run of 340 ns was then performed to comprehensively sample the intramolecular degrees of freedom. An average calculation was performed on 6 $\times$ 2.2 GHz Intel Xeon E5-2430 CPU cores, achieving execution speeds of $\sim$1100 ns/day for the optimal model selected by our procedure.

Monomer and dimerization potentials of mean force. Potentials of mean force for the reparameterized coarse-grained model and the original Martini model were computed in an identical manner to those described for the all atom model in Section 2.1.1, with umbrella potentials applied to the beads containing the terminal carbon atoms (Fig. 1).

2.1.4. Validation of coarse-grained model

We assess and validate the performance of the reparameterized coarse-grained model in reproducing the bonded distribution functions, all-atom monomer collapse PMF, dimerization PMF, and contact map. A complete listing of the coarse-grained bonded and non-bonded parameters is provided in Tables S1-S8 in the Supporting Information, and in the tabulated force field files `b0-b8.txt` and `a0-a12.txt` and the DFAG coarse-grained topology `topology.txt` provided as Supplementary Files.

Bonded distributions. It is important that the bonded distributions of a coarse-grained model be in good agreement with the all-atom results in order to accurately reproduce the internal bonded structure of the molecule. Coarse-grained simulations of the original Martini model showed relatively poor agreement with the all-atom calculations, and we improved the quality of the coarse-grained model by reparameterizing the bonded interactions using

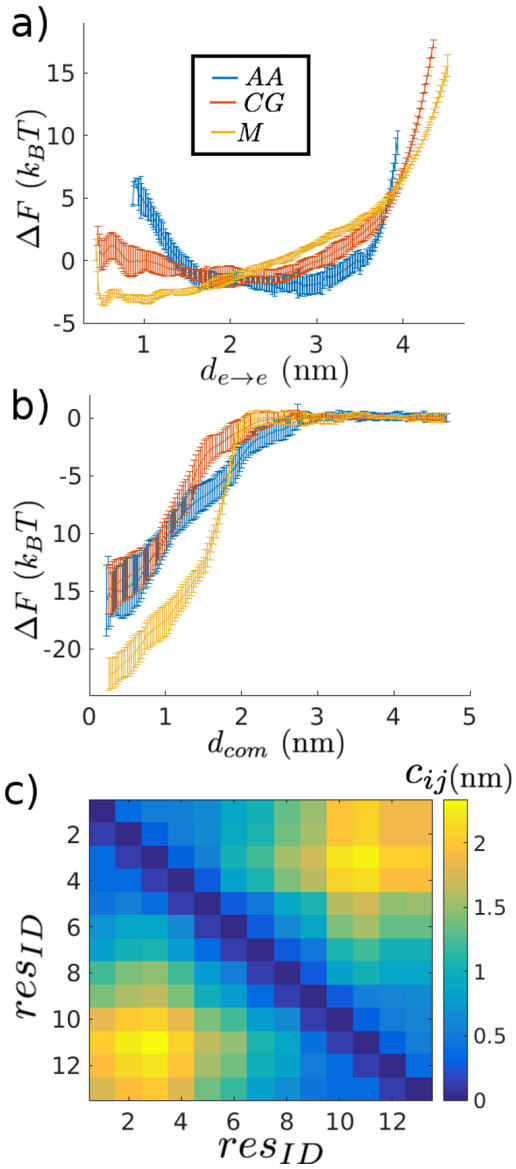

Figure 2: Validation of the reparameterized coarse-grained model. (a) Monomer collapse PMFs for all-atom (AA), reparameterized coarse-grained (CG), and original Martini (M) models. $d_{e\to e}$ represents the distance between the terminal carbon atoms or the beads containing the terminal carbon atoms, and ΔF is the (relative) Gibbs free energy determined by umbrella sampling. The arbitrary additive constant specifying the vertical offset of each PMF profile was specified for the all-atom model such that ΔF averaged over the profile is zero, and for the two coarse-grained models to minimize the point-wise root-mean-square distance m_{rms} relative to the all-atom profile (cf. Eqn. 2). (b) Dimerization PMFs for the all-atom, reparameterized coarse-grained, and original Martini models. d_{com} represents the center of mass distance between the two monomers and ΔF is the (relative) Gibbs free energy determined by umbrella sampling. The arbitrary additive constant specifying the vertical offsets of the PMF profiles were specified by aligning the plateau regions at large separations corresponding to effectively non-interacting monomers to $\Delta F = 0\ k_BT$. (c) Time-averaged contact maps of the all-atom (lower triangle) and reparameterized coarse-grained (upper triangle) models.

the Boltzmann inversion procedure detailed in Section 2.1.2. In Figs. S1-S5 of the Supplementary Information, we present a comparison between the 33 bond, 24 angle, 15 proper dihedral, and 2 improper dihedral distributions sampled by the all-atom and reparameterized coarse-grained models. In all cases, the reparameterized coarse-grained model adequately recapitulates the range and character of the bonded distribution functions, with the exception of 6/33 bonds (Fig. S1e-j) and 9/24 angles (Fig. S3a,d,e,l,m,q-t) where it fails to precisely reproduce bimodalities observed in the all-atom calculations. This should be regarded as a deficiency of the reparameterized coarse-grained model that could be ameliorated by more sophisticated inversion techniques such as iterative Boltzmann inversion or inverse Monte-Carlo[26,53], or more extensive modifications of the functional forms of the bonded and angle potentials in addition to retuning of the parameters. Nevertheless, the overall agreement of the coarse-grained and all-atom bonded distributions is quite good, a substantial improvement over the original Martini model, and sufficient to accurately reproduce the thermodynamic and structural properties described below.

Monomer collapse PMFs. In Fig. 2a, we present PMF curves quantifying the free energy of a monomer in solution as a function of its end-to-end distance computed from the all-atom, original Martini, and reparameterized coarse-grained models. Accurate reproduction of the all-atom PMF by a coarse-grained model is a prerequisite to realistic modeling of the equilibrium distribution between extended and collapsed configurations of a single peptide. It is apparent from the PMF curves that the original Martini model poorly reproduces the distribution of end-to-end distances observed in the all-atom simulations, whereas our coarse-grained model constructed by reparameterizing the bonded Martini interactions and incorporating backbone proper dihedrals exhibits greatly improved agreement. Specifically, the all-atom PMF exhibits a flat-bottomed character in which the free energy is essentially flat within error bars over the region 1.6 to 3.2 nm. Our coarse-grained model reproduces this feature, possessing a flat bottom over the range 1.3 to 2.8 nm that is shifted relative to the all-atom model by only $\sim$0.3 nm, marginally favoring slightly more collapsed configurations.

In contrast, the original Martini model excessively favors highly collapsed peptide configurations, exhibiting a flat-bottomed minimum over the range 0.5 to 1.1 nm that is completely outside the range of that for the all-atom model. Outside of the flat-bottomed minimum, our coarse-grained model also significantly better reproduces the wings of the distribution relative to the original Martini model, but the agreement is not quantitative. Specifically, for end-to-end distances in the range 0.5 to 1.5 nm, the reparameterized coarse-grained model under-predicts the all-atom PMF, leading to an elevated preference for collapsed peptide configurations. Conversely, over the range 1.5 to 3.8 nm the coarse-grained PMF lies above that of the all-atom model, leading to a slightly suppressed preference for moderately extended conformations in the coarse-grained model, but this trend inverts in the region above 3.8 nm such that highly extended conformations are slightly more favored. Nevertheless, the agreement between the reparameterized coarse-grained and all-atom models is very good over the flat-bottomed minimum, and differs outside this region by $\sim$5 k_BT such that discrepancies in the relative stabilities of the collapsed and extended conformations predicted by the two models are within only a few multiples of the scale of thermal fluctuations.

We quantify the agreement between the reparameterized coarse-grained and all-atom PMFs using the point-wise root-mean-square distance between the optimally-aligned PMF profiles,

$$m_{rms} = \frac{1}{N}\sqrt{\sum_{i=1}^{N}(M_i^{AA} - \widetilde{M}_i)^2}, \tag{2}$$

where M^{AA} is the all-atom PMF and $\widetilde{M}$ is the coarse-grained PMF, optimally shifted relative to M^{AA} to minimize m_{rms} (i.e., specifying the arbitrary additive constant in the PMF to minimize the point-wise RMSD), and linearly interpolated at the $i = 1...N$ points at which M^{AA} was computed. Our reparameterized coarse-grained model better reproduces the all-atom distribution ($m_{rms}^{CG} = 0.14$ k_BT per point) compared to the unmodified Martini model (m_{rms}^{M}= 0.24 k_BT per point), corresponding to an average 42% improvement in the per point agreement of the PMF curves. The substantially improved agreement of our coarse-grained

PMF relative to the original Martini model demonstrates the importance and value of explicit reparameterization against all-atom data. Moreover, it is notable that the reparameterized coarse-grained model uses identical non-bonded parameters to the original Martini model, and that this elevation in performance emerges exclusively from reparameterization of the bonded interactions and is not due to direct fitting of the monomer collapse PMF.

Dimerization PMFs. In Fig. 2b, we present dimerization PMF curves quantifying the free energy as a function of the center of mass distance between a pair of monomers calculated using the all-atom, original Martini, and reparameterized coarse-grained models. In each case, we explicitly remove the trivial entropic contribution arising from restraining two objects to reside at a particular separation[58]. Reproduction of the all-atom dimerization PMF by a coarse-grained model is critical in properly modeling the strength and character of the pairwise interactions between monomers that mediate peptide assembly. The all-atom PMF reveals a relatively strong thermodynamic driving force for dimerization of $\Delta F^{AA} = (16 \pm 3)\ k_B T$, as measured from the plateau region at center of mass separations in excess of $\sim$3 nm, corresponding to essentially non-interacting monomers, to the global minimum at $\sim$0.25 nm, representing the dimer contact pair. The original Martini model predicts $\Delta F^{M} = (22 \pm 1)\ k_B T$, overestimating the driving force for dimerization by 38%. The prediction of the reparameterized coarse-grained model of $\Delta F^{CG} = (15 \pm 2)\ k_B T$ is in excellent agreement with the all-atom calculations. The shape of the curve along the dimerization pathway is also in quite good agreement, although the coarse-grained model slightly overestimates the all-atom PMF by a maximum of $\sim$4 $k_B T$ for center of mass separations in the range 1.5 to 2.0 nm. Again, it is notable that this agreement emerges from reparameterization of only the bonded interactions and is not due to direct fitting of the dimerization PMF.

We again quantify the difference in the all-atom and reparameterized coarse-grained PMFs using the point-wise root-mean-square distance between the optimally-aligned dimer-

ization PMF profiles,

$$d_{rms} = \sqrt{\sum_{i=1}^{N} (D_i^{AA} - \widetilde{D}_i)^2}, \tag{3}$$

where D^{AA} is the dimer all-atom profile and $\widetilde{D}$ is the dimer coarse-grained profile linearly interpolated at the $i = 1...N$ points at which D^{AA} was computed. In this case, the arbitrary additive constant for each PMF was specified by aligning the plateau regions of the two PMFs at large monomer separations, corresponding to effectively non-interacting monomers. The modified coarse-grained model provides a much more accurate reproduction of the all-atom PMF ($d_{rms}^{CG} = 0.10$ k_BT per point) compared to the unmodified Martini model ($d_{rms}^{M} = 0.27$ k_BT per point), an average 62% improvement in the per point agreement of the PMF curves.

Contact maps. In Fig. 2c, we present a comparison of the contact maps computed from our all-atom and reparameterized coarse-grained models. The all-atom contact map C^{AA} was computed as the time-averaged pairwise distances between the centers of mass of the thirteen residues of the all-atom system of an isolated DFAG peptide simulated in water for 340 ns (cf. Section 2.1.1), and the coarse-grained contact map C^{CG} as the time-averaged pairwise distances between the centers of mass of the corresponding thirteen residues of the coarse-grained system of an isolated DFAG peptide simulated in water for 340 ns (cf. Section 2.1.3). Contact maps provide a time-averaged measure of relative residue positions and therefore quantify differences in intramolecular structure[36]. It is critical that a coarse-grained model accurately recapitulate the all-atom contact map in order to properly reproduce the peptide secondary structure. Visual comparison of the two contact maps shows good agreement between the two models, indicating that the reparameterized coarse-grained model properly recapitulates the internal structure of the all-atom peptide. It is visually apparent that neighboring residues in the coarse-grained model tend to be slightly further separated than in the all-atom calculations, but no pair of residues over the entire peptide is in disagreement by more than ∼0.5 nm. To provide a global comparative measure of pairwise residue distances in the all-atom and coarse-grained systems, we compute the Frobenius norm of the difference

of the contact map matrices,

$$d_{cmap}^{CG} = \sqrt{\sum_{i=1}^{r_{num}} \sum_{j=1}^{r_{num}} (c_{ij}^{AA} - c_{ij}^{CG})^2}, \tag{4}$$

where $r_{num} = 13$ is the number of residues (four amino acid residues in each wing, two C-termini, and three OPV3 aromatic rings; see Fig. 1), c_{ij}^{AA} is the (i, j)th element in the all-atom contact map matrix C^{AA}, and c_{ij}^{CG} is the (i, j)th element in the coarse-grained contact map matrix C^{CG}. The resultant value $d_{cmap}^{CG} = 1.98$ nm indicates that on average the coarse-grained contact map differs from the atomistic by only $d_{cmap}^{CG}/N^2 = 0.012$ nm/residue, indicating globally good agreement of the secondary structure predicted by the two models.

Summary. Overall, the reparameterized coarse-grained model satisfactorily reproduces the all-atom bonded distribution functions, monomer collapse PMF, dimerization PMF, and contact maps. Although the standard Martini potential has been previously profitably employed to study self-assembly of small peptides[35], it is notable that by incorporating backbone proper dihedrals and reparameterizing the bonded interactions using all-atom data, the modified model demonstrates substantial improvements in recapitulating the dimerization PMF and secondary structure predictions that are important features governing self-assembly[36]. This enhancement illustrates the value of this approach in tailoring the coarse-grained model for a particular peptide chemistry to elevate predictive performance and offers an extensible means to develop coarse-grained models for other peptide chemistries. The coarse-grained model does, however, possess two non-trivial deficiencies. First, it does not properly resolve bimodalities in several bonds and angles observed in all-atom calculations, although this occurs for only a relatively small fraction of the bonded distribution functions and does not compromise the global structural and thermodynamic properties assessed by the monomer and dimer PMFs and contact maps. Second, the coarse-grained model overly favors collapsed peptide conformations relative to the all-atom calculations, but the discrepancy is on the order of $\sim$5 k_BT such that the effect is rather mild. In both cases, we observe that agree-

ment could be improved by using more sophisticated reparameterization procedures[26,53], modification of the functional forms of the bonded potentials, or by reparameterization of the non-bonded interaction parameters. Finally, the reparameterized model offers ∼25× speedups relative to all-atom calculations, allowing us to probe self-assembly up to hundreds of monomers and hundreds of nanoseconds to reach time and length scales inaccessible to atomistically-detailed simulations.

2.2 Coarse-grained molecular dynamics simulations of self-assembly

The coarse-grained model detailed in Section 2.1.2 permits us to access the time and length scales necessary to observe spontaneous peptide self-assembly in coarse-grained molecular dynamics simulations of hundreds of DFAG-OPV3-GAFD oligopeptides in water over hundreds of nanoseconds. Calculations were conducted in the Gromacs 4.6 simulation suite[56]. Initial peptide configurations were constructed from coarse-grained mappings from structures harvested from the all-atom calculations. Simulations were conducted in the NPT ensemble at 298 K and 1 bar, employing a velocity rescaling thermostat[57], a Parrinello-Rahman barostat[43], and three-dimensional periodic boundary conditions. Initial bead velocities were randomly assigned from a Maxwell-Boltzmann distribution at 298 K, and high energy overlaps in the initial configurations eliminated by performing steepest descent energy minimization to remove forces exceeding 1000 kJ/mol-nm. Equations of motion were numerically integrated using a leap-frog algorithm[44] with a 5 fs time step, and constrained bond lengths fixed using the LINCS algorithm[45]. Lennard-Jones interactions were shifted smoothly to zero at 1.1 nm. Electrostatic interactions were treated using reaction field electrostatics and a relative electrostatic screening of 2.5 for polarizable water (deprotonated, high-pH model) and 15 for non-polarizable water (protonated, low-pH model). Calculations were performed on 12 × 2.2 GHz Intel Xeon E5 CPU cores and 2 × NVIDIA Tesla M7020 GPUs, achieving execution speeds on the order of ∼150 ns/day.

2.2.1. Deprotonated (high pH) simulations.

Simulations of 343 deprotonated (-4 net charge) DFAG-OPV3-GAFD molecules were initialized by placing the oligopeptides in random locations with random orientations in an initially $33 \times 33 \times 33$ nm^3 box. Charge neutrality was maintained by 1372 randomly placed counter ions represented by Martini Qd beads each carrying a +1 charge[22] and the system solvated with Martini polarizable water[55] to a achieve a peptide concentration of 15 mM. Experimentally, there is evidence that peptides do not form large aggregates under high pH conditions[16–19], but that they may form small aggregates such as dimers or trimers[59]. The system was subjected to a 300 ns equilibration run to allow the cluster size distribution to attain a steady value, before conducting a single 100 ns production run over which we harvested equilibrium statistics.

2.2.2. Protonated (low pH) simulations.

Simulations of 42, 126, 200, 252, and 378 protonated (electrically neutral) DFAG-OPV3-GAFD molecules were prepared by insertion at random locations in random orientations into $23.5 \times 23.5 \times 23.5$ nm^3 boxes and solvated with Martini non-polarizable water[51] to achieve average molar concentrations of 5.0 mM, 15 mM, 24 mM, 30 mM, and 44 mM, respectively. Each system was initially subjected to a short 50 ps run to allow the energy, temperature, and pressure to attain stable values before commencing 5×400 ns independent production runs in which we observed spontaneous and irreversible peptide aggregation. Experimentally, DFAG-OPV3-GAFD oligopeptides are known to aggregate under low pH conditions at concentrations exceeding 10^{-3} mM[18], and have been studied at concentrations up to 0.86 mM[19]. We perform simulations at six-fold larger concentrations and higher to robustly observe assembly of hundreds of peptides over hundreds of nanoseconds. We demonstrate below that the aggregation mechanism is concentration independent over the range of values considered in this work.

For direct comparison with the deprotonated (high pH) simulations, we also conducted

a simulation of 343 protonated (low pH) molecules in a $33 \times 33 \times 33$ nm^3 box solvated with Martini non-polarizable water[51] at a concentration of 15 mM. It was initially subjected to a short 50 ps run to allow the energy, temperature, and pressure to attain stable values before commencing a 1.3 μs production run.

2.2.3. Time scale correspondence in all-atom and coarse-grained simulations

It is well known that coarse-graining can artificially accelerate the system dynamics by eliminating degrees of freedom and smoothing the underlying free energy landscape, and that different dynamical degrees of freedom may be accelerated by different scaling factors[37,51,60]. Since it is peptide self-assembly that is of the most interest to us, the relevant dynamical time scale is the center of mass peptide translation that governs the rate at with which the molecules come into contact with one another. Accordingly, we ascertain the coarse-graining speedup by comparing the translational self-diffusion coefficients of the all-atom and coarse-grained DFAG-OPV3-GAFD molecules[20,61–63]. Using the same simulation procedures as described in Section 2.1.1 and Section 2.2.2, we conducted a 10 ns simulation of an isolated peptide in a $7 \times 7 \times 7$ nm^3 simulation box employing both the all-atom and coarse-grained models. We computed the self-diffusion coefficients by calculating the mean squared displacement of the peptide center of mass and applying the Einstein relation[64]. Uncertainties were estimated by blocking the trajectory into 20 equally sized segments and computing the standard deviation of the self-diffusion coefficients calculated over these blocks. We determine a self-diffusion coefficient in the coarse-grained runs of $D_{CG} = (7 \pm 2) \times 10^{-6}$ cm^2/s compared to $D_{AA} = (12 \pm 3) \times 10^{-6}$ cm^2/s in the all-atom calculations. Interestingly, we observe a slight slowing down of the coarse-grained dynamics, which has previously been observed for Martini representations of certain molecules including alkane chains[37]. Nevertheless, the self-diffusion coefficients agree within error bars, indicating that there is no significant difference in the dynamical time scales of the two simulations. Accordingly, we apply no rescaling corrections to the coarse-grained simulation time scale.

2.3 Metrics to define a hierarchy of cluster types with different aggregation morphologies

Overlap and delocalization of the π-orbitals in the OPV3 cores of the oligopeptides within supramolecular aggregates endows these assemblies with emergent optoelectronic functionality[11]. The structural arrangement of the OPV3 cores is therefore of primary interest in characterizing the observed self-assembled aggregates. Following metrics previously developed to define clusters in asphaltene aggregation[65], we define three criteria to determine whether or not two oligopeptides should be considered to exist in the same aggregate. The metrics, in increasing degree of strictness, are described below and illustrated schematically in Fig. 3.

Metric 1 – Contact clusters. Metric 1 defines the distance between two oligopeptides a and b as,

$$R^{(1)}_{a,b} = \min_{i \in a} \min_{j \in b} r_{ij}, \tag{5}$$

where r_{ij} is the distance between beads i and j, and the minimization is taken over all beads in each molecule. We define "contact clusters" to be clusters comprised of pairs of molecules that satisfy $R^{(1)}_{a,b} < r^{(1)}_{\text{cut}}$, where $r^{(1)}_{\text{cut}}$ is a tunable cutoff distance that is discussed below. Two molecules are therefore considered to be in a contact cluster if any two of their constituent atoms are within the cutoff distance of each other. Contact clusters would not necessarily be expected to demonstrate desirable optoelectronic properties, as their cores may or may not possess the π-π stacking necessary for electronic delocalization.

Metric 2 – Optical clusters. Metric 2 defines the distance between two oligopeptides a and b as,

$$R^{(2)}_{a,b} = \min_{i \in (\text{core } a)} \min_{j \in (\text{core } b)} r_{ij}, \tag{6}$$

where r_{ij} is the distance between the centers of mass of aromatic rings i and j, and the minimization proceeds over the three aromatic rings within the OPV3 core of each molecule.

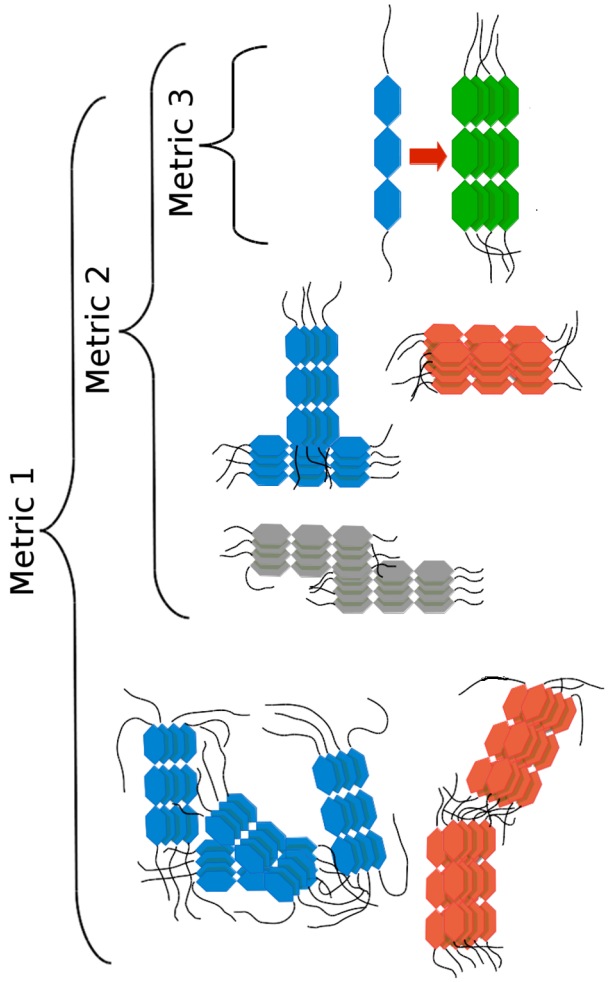

Figure 3: A schematic illustration of the hierarchy of cluster types as defined by Metrics 1, 2, and 3. Metric 3 defines an "aligned cluster," which is made up of molecules with aligned aromatic cores. Metric 2 defines an "optical cluster," composed of aligned clusters with interacting, but not necessarily aligned, aromatic cores. Metric 1 defines a "contact cluster," which is made up of optical clusters interacting by promiscuous and non-specific side chain and core contacts. The distinct clusters defined by each metric are identified in different colors.

We define "optical clusters" to be clusters comprised of pairs of molecules that satisfy $R^{(2)}_{a,b} < r^{(2)}_{\text{cut}}$. Two molecules are considered to be in an optical cluster if the minimum distance between any two aromatic rings is within the cutoff. This metric assures proximity of the aromatic rings between the two molecules, and we term these aggregates optical clusters since this proximity can lead to electronic delocalization and the emergence of optoelectronic properties.

Metric 3 – Aligned clusters. Metric 3 defines an associated distance between any two molecules a and b as,

$$R_{a,b}^{(3)} = \max\left[\left(\max_{i\in(\text{core } a)}\min_{j\in(\text{core } b)} r_{ij}\right), \left(\max_{i'\in(\text{core } b)}\min_{j'\in(\text{core } a)} r_{i'j'}\right)\right], \tag{7}$$

where r_{ij} is the distance between the centers of mass of aromatic rings i and j, and the minimization and maximization are taken over three aromatic rings within the OPV3 core of each molecule. We define "aligned clusters" to be clusters comprised of pairs of molecules that satisfy $R_{a,b}^{(3)} < r_{\text{cut}}^{(3)}$. The first term in the square brackets computes the minimum distance from each aromatic ring center of mass i in molecule a to any aromatic ring center of mass j in molecule b, and returns the largest of these distances[65]. The second term inverts the order of a and b since the maximin operation does not commute. As previously observed[65], this "longest shortest distance" is analogous to the mathematical definition of the diameter of a graph[66]. Accordingly, two molecules a and b are in an aligned cluster if the maximum of all minimum distances between any aromatic ring in a and any aromatic ring in b is within the cutoff. Pairs of molecules that meet this requirement possess OPV3 cores that are well aligned, and aggregates defined according to this metric are expected to exhibit the strongest optoelectronic properties.

Cutoff distances. Following Thurston et al.[20], we employed a cutoff for Metric 1 $r_{\text{cut}}^{(1)} = 0.5$ nm defined to be close to the minimum of the Lennard-Jones potential for larger atoms in the atomistic model. To determine the cutoff for the Metrics 2 and 3 that explicitly considers aromatic ring interactions, we simulated a coarse-grained contact dimer of two protonated (low pH) DFAG-OPV3-GAFD peptides in water over the course of 30 ns using the simulation parameters detailed in Section 2.2.2. We compiled histograms of the distances between each aromatic ring center of mass and its nearest neighbor in the other molecule comprising the dimer, and specified our cutoffs as the mean of this distribution $r_{\text{cut}}^{(2)} = r_{\text{cut}}^{(3)} = 0.7$ nm.

Nesting of metrics. We observe that the metrics are nested such that a pair of peptides

identified as an aligned cluster (Metric 3) will also be identified as an optical cluster (Metric 2) and a contact cluster (Metric 1), and a pair identified as an optical cluster is also identified as a contact cluster. The inverse, however, is not true. A pair of peptides identified as a contact cluster may or may not be an optical or aligned cluster. Accordingly, for any group of peptides the contact cluster size is constrained to be equal to or greater than the optical cluster size, which in turn is constrained to be equal to or greater than the aligned cluster size.

3. RESULTS AND DISCUSSION

3.1 Morphological characterization of hierarchical self-assembly

We have constructed a coarse-grained model of DFAG-OPV3-GAFD π-conjugated oligopeptides explicitly parameterized against all-atom simulation data. This efficient model allows us to directly simulate the spontaneous self-assembly of hundreds of peptides over hundreds of nanoseconds, allowing us to characterize the molecular-level morphology and kinetics of early-stage assembly of optically-active aggregates.

3.1.1. Assembly of deprotonated (high pH) molecules is self limiting

It is known from experiment that deprotonated (high pH) DFAG-OPV3-GAFD molecules do not assemble large aggregates due to electrostatic repulsion between their negatively charged Asp termini[16,17,19], although there is recent experimental[59] and computational[20] evidence that the formation of small aggregates is thermodynamically spontaneous due to favorable dispersion, π-stacking, and hydrophobic interactions. Our simulations of deprotonated peptides at 15 mM corroborate this result, showing the cluster size distributions under each of the three cluster metrics (cf. Section 2.3) do attain stable equilibrium distributions within 300 ns of simulation (Fig. 4a). This observation corresponds to the self-limiting aggregation of peptides into small aligned and optical clusters containing up to five monomers, and small

contact clusters containing up to eight. The high concentration of negative charge within these small aggregates supplied by the deprotonated Asp termini prohibits further assembly into larger aggregates.

3.1.2. Assembly of protonated (low pH) molecules is hierarchical and irreversible

We present in Fig. 5 the mass-averaged cluster size of the contact, optical, and aligned clusters as a function of time for each of the five concentrations considered under protonated (low pH) conditions. Contact clusters (Metric 1) exhibit irreversible aggregation that leads to the formation of increasingly large aggregates over the course of our 400 ns production runs. Aggregation initially occurs by the aggregation of monomers, but at later times proceeds by the agglomeration of peptide aggregates, and proceeds more rapidly at higher concentrations. In Fig. 4b we present the time resolved contact cluster size distribution at 15 mM. These observations are consistent with experimental data showing the irreversible assembly of up to micron sized aggregates under low pH conditions[16–18,59].

Optical clusters (Metric 2) also exhibit irreversible and unbounded aggregation. At 5.0 mM, we observe little difference in the average size of contact and optical clusters, which indicates that optical clusters are not associating into larger contact clusters through side chain interactions over the 400 ns simulation time scales. At higher concentrations, the optical cluster size is substantially smaller than that of the contact clusters, indicating the presence of higher order association through side chain interactions. We observe an initially rapid formation rate of optical clusters that yields to a much slower aggregation rate at ∼200 ns and an average cluster size of ∼5-10 molecules, which indicates a cluster size dependent mechanism of aggregation. Larger optical clusters are both less mobile and have less favorable surface area through which to form new optical clusters. Optical clusters also form by rearrangements or "ripening" of contact clusters to form the more energetically favorable optical clusters. In Fig. 4c we present the time resolved optical cluster size distribution at 15 mM.

Contrary to the unbounded growth of contact and optical clusters, aligned clusters (Metric 3) do exhibit self-limiting behavior. After ∼200 ns for all concentrations studied, we observe the emergence of a mass-averaged cluster size of aligned clusters of $\mu_2^{\text{aligned}} \approx 2$. In Fig. 4d we present the aligned cluster size distribution at 15 mM, which reveals a decreasing distribution in aligned cluster sizes up to a maximum size of 8. The most probable aligned cluster size is a monomer, with 30% of peptides existing in this state. Dimers, trimers, and tetramers account for 25%, 22%, and 11% of peptides, respectively, leaving only 12% as higher order aligned aggregates.

Our results reveal a hierarchical assembly mechanism at low pH, wherein peptides rapidly achieve a steady-state distribution of aligned clusters comprised of ordered stacking between all three aromatic rings in the OPV3 cores. This distribution is dominated by small cluster sizes, with 88% of peptides in aligned clusters existing as monomers, dimers, trimers, or tetramers. These aligned clusters form the components of larger optical clusters formed from proximate interactions between the aromatic cores, but lacking the in-register stacking and alignment of the aligned clusters. Contrary to the aligned clusters, the optical clusters do not attain a steady-state cluster size distribution, but continue to increase in size over the entire simulation, both by agglomeration with other optical clusters and internal rearrangements in which portions of contact clusters ripen into optical clusters through improved ordering and stacking of the constituent monomers. Nevertheless, beyond ∼200 ns this growth is relatively slow, and the mass-averaged optical cluster size in the time window 200-400 ns is $\mu_2^{\text{optical}} \approx 10$. These optical clusters, in turn, serve as the building blocks for still larger contact clusters that are formed by promiscuous and non-specific contacts between optical cluster side chains and cores. Contact clusters also grow without bound, assembling by irreversible agglomeration to ultimately subsume all peptides in the system. We present in Fig. 6 representative snapshots of the latter stages of assembly at each of the concentrations studied.

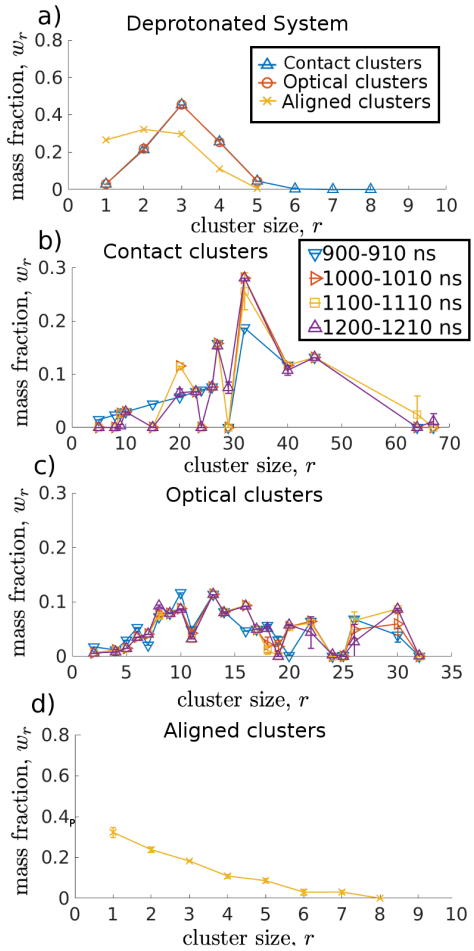

Figure 4: Cluster size distributions in the deprotonated (high pH) and protonated (low pH) systems at 15 mM. (a) Mass fraction w_r of peptides in the deprotonated (high pH) system that exist in clusters of size r defined according to the three metrics. The mass fraction distributions under all three metrics cease to evolve within the 300 ns equilibration period simulation time, indicating that the aggregation process has attained a dynamic equilibrium, and data are averaged over the 100 ns production run. In the protonated (low pH) state, the mass fraction distributions for aligned clusters reaches steady state after ∼200 ns, but the optical and contact cluster distributions never reach a terminal distribution and continue to shift to larger cluster sizes over the course of the entire 1.3 μs production run, indicating unbounded and irreversible aggregation, although the process is rather slow for this concentration. (b) Mass fraction distribution of protonated (low pH) contact clusters averaged over the four time windows 900-910 ns, 1000-1010 ns, 1100-1110 ns, and 1200-1210 ns. (c) Mass fraction distribution of protonated (low pH) optical clusters averaged over the four time windows 900-910 ns, 1000-1010 ns, 1100-1110 ns, and 1200-1210 ns following the legend in panel (b). (d) Steady state mass fraction distribution of aligned clusters in the protonated (low pH) state averaged over the terminal 100 ns of the production run. Uncertainties in all cases correspond to standard errors estimated by block averaging. Error bars not explicitly displayed are smaller than symbol size. Lines connecting the points are provided to guide the eye.

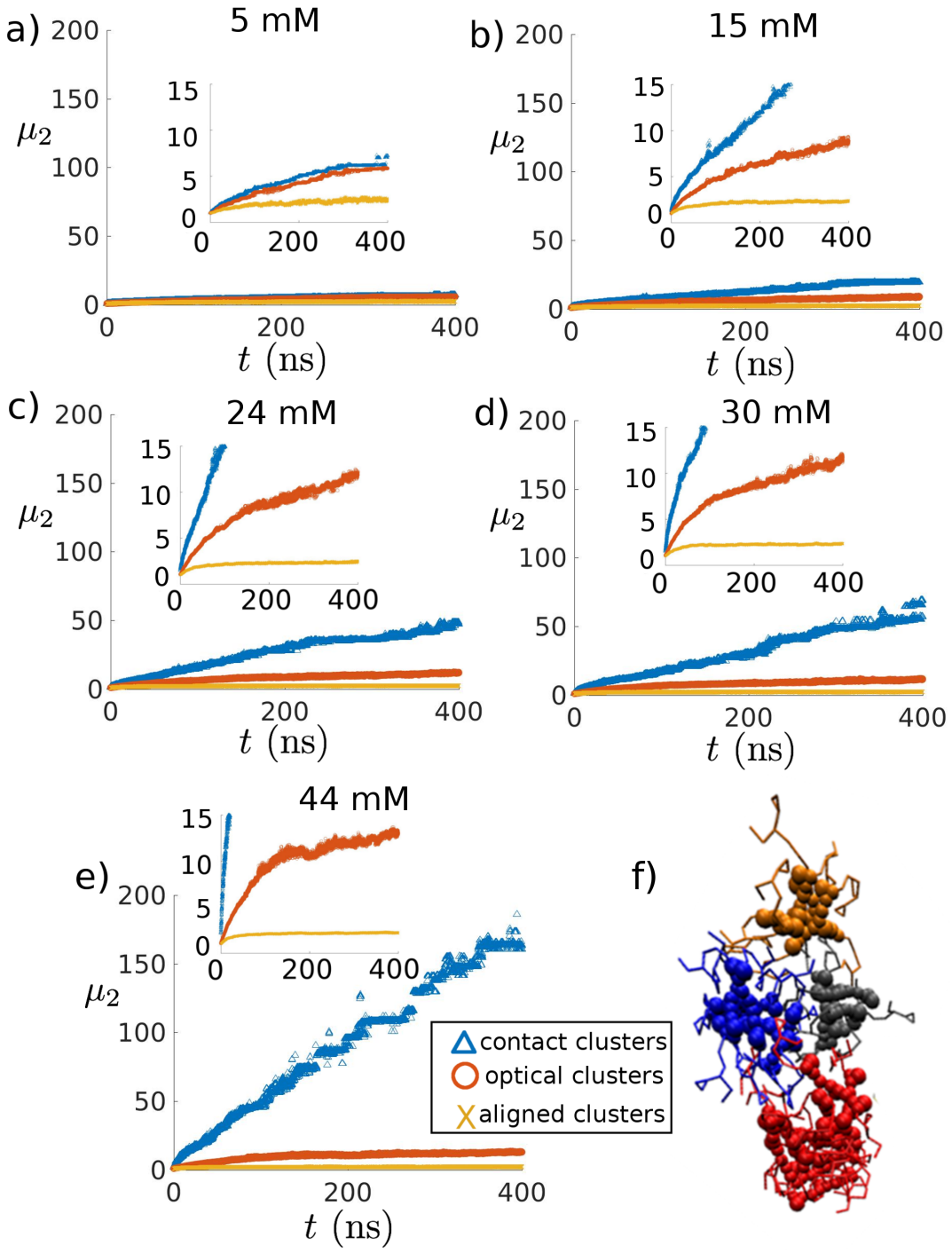

Figure 5: The mass-averaged cluster size as a function of time according to the three cluster metrics for the protonated (low pH) system at concentrations of (a) 5.0 mM, (b) 15 mM, (c) 24 mM, (d) 30 mM, and (e) 44 mM, where all panels follow the legend displayed in panel (e). Systems were initialized from randomly oriented and randomly placed monomers. The insets show a zoom on optical and aligned clusters. (f) A representative snapshot of a contact cluster in which the constituent optical clusters are distinguished by different colors. All molecular visualizations in this work were constructed using VMD[67].

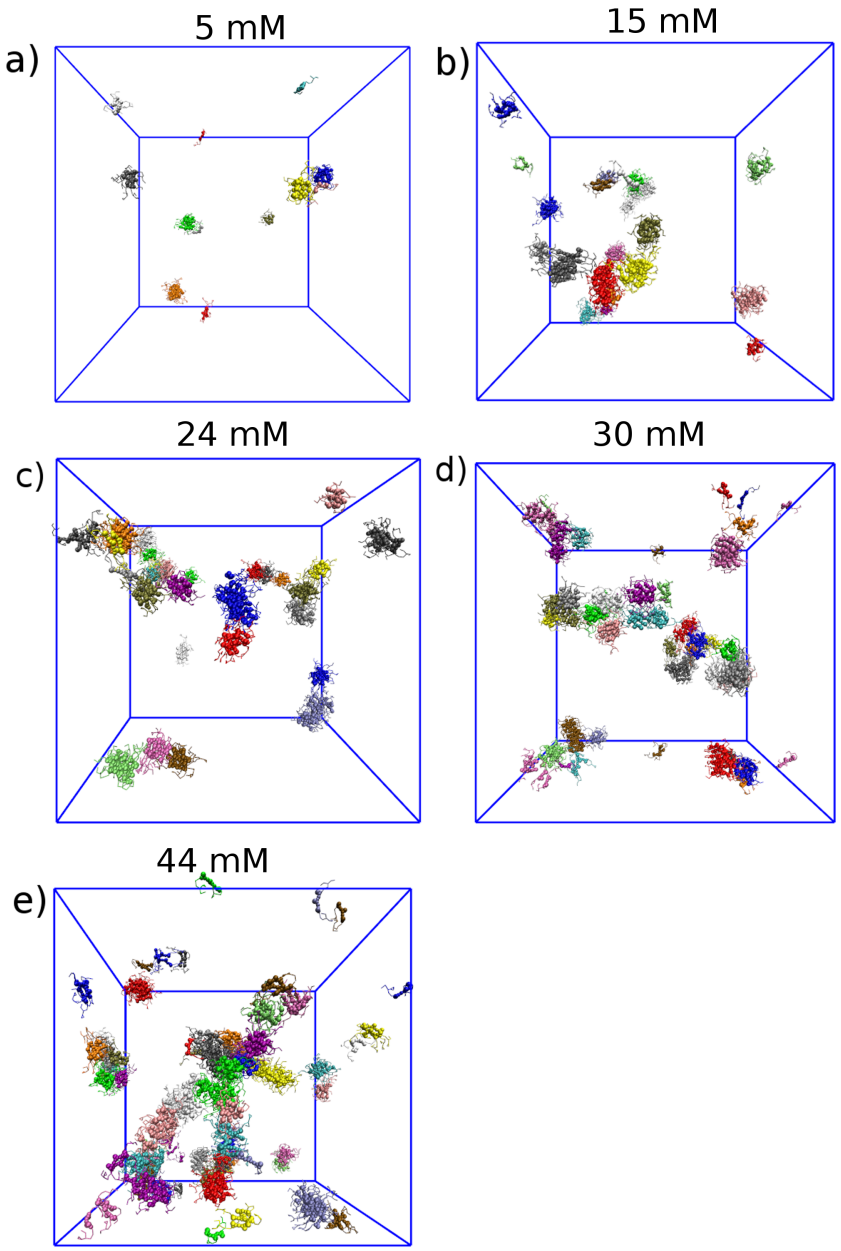

Figure 6: Representative snapshots of the late-stage (>200 ns) assembly of the protonated (low pH) peptides at concentrations of (a) 5.0 mM, (b) 15 mM, (c) 24 mM, (d) 30 mM, and (e) 44 mM. At this time, the aligned cluster size distribution has attained steady state. The optical cluster size distribution continues to move towards larger cluster sizes relatively slowly through agglomeration and internal rearrangements of contact clusters. Contact clusters form by unbounded and irreversible agglomeration, and by this time most of the aggregation in the system occurs through agglomeration of optical clusters containing >10 peptides. For ease of viewing, in each panel we have indicated the distinct optical clusters in a different color, where core beads are represented as spheres, side chains as lines, and water has been removed for clarity.

3.1.3. Contact clusters are fractal aggregates

To characterize the morphology of the self-assembling contact clusters of protonated (low pH) peptides defined according to Metric 1, we estimate the fractal dimensionality of the system at different scales by computing the correlation dimension. The correlation dimension D is a measure of the space-filling nature of a system, and is estimated from the correlation integral $C(r)$[68]. For a set of N points in space, the correlation integral is defined as,

$$C(r) = \lim_{N\to\infty} \frac{g}{N^2}, \tag{8}$$

where g is the number of pairs of points separated by a distance less than r[68]. The fractal dimension is related to the correlation integral through the relationship,

$$C(r) \sim r^D, \tag{9}$$

which provides a measure of how rapidly new points are accumulated into an expanding sphere around a tagged point. We numerically estimate the correlation integral for our system as[65,69],

$$C(r) = \frac{1}{N(N-1)} \sum_{\substack{i,j=1 \\ i\neq j}}^{N} H(r - r_{ij}^{\mathrm{COM}}), \tag{10}$$

where r_{ij}^{COM} is the distance between the centers of mass of monomers i and j, and $H(x)$ is the Heaviside step function,

$$H(x) = \begin{cases} 0 & x < 0 \\ 1 & x \geq 0. \end{cases} \tag{11}$$

In Fig. 7a-e, we present the log-log plot of $C(r)$ versus r for the final snapshot of the five independent runs conducted at each concentration. In each case, we observe approximately three regimes: the first spanning ∼0.13-1.0 nm, the second ∼1.0-7.4 nm, and the third ∼7.4-20 nm. The shortest length scale regime approximately corresponds to the characteristic size

of aligned and optical clusters in the system (cf. Fig. 9a), the medium length scale regime to smaller contact clusters containing ∼3-5 optical clusters (cf. Fig. 9b), and the longest length scale regime to large contact clusters which saturates at large ℓ due to the finite size of the simulation box (cf. Fig. 9c). At the lowest 5 mM and 15 mM concentrations, the second regime comprises largely the interstitial solvent between isolated aggregates as demonstrated by the flat nature of $C(\ell)$, and the third regime characterizes the characteristic separations between these clusters (cf. Fig. 6a-b). At higher concentrations, the peptides begin to form a connected network, and $C(\ell)$ possesses a positive slope at all length scales (cf. Fig. 6c-e).

In Fig. 7f, we present the fractal dimension extracted from linear fits constructed within each of the three regions as a function of concentration. In the first region, the fractal dimension is ∼2 for all concentrations studied, corresponding to the growth of small aligned and optical clusters into slightly elongated ellipses (cf. Fig. 9a). The second region has a fractal dimension that grows with concentration, from ∼0.5 to ∼1.5 corresponding to the departure from isolated aligned and optical clusters to the formation of increasingly large contact clusters. The third region has a fractal dimension of ∼1.5 for all concentrations, reflecting the formation of a fractal network of branched contact clusters (cf. Fig. 9c).

3.1.4. Contact clusters assemble asymmetrically into elongated ellipsoidal aggregates that display branching behavior

To further characterize and explore the three structural regimes identified in the analysis of the fractal dimension, we computed the gyration tensor $\mathbf{S}$ for each contact cluster defined according to Metric 1 observed in our simulations as[70],

$$\mathbf{S}_{pq} = \frac{1}{2R^2} \sum_{i=1}^{R} \sum_{j=1}^{R} (r_p^{(i)} - r_p^{(j)})(r_q^{(i)} - r_q^{(j)}), \tag{12}$$

where p and q index over the three Cartesian coordinates $\{x, y, z\}$, i and j index over the beads of all peptides in the cluster, $R = 29r$ is the total number of beads in the cluster, r is

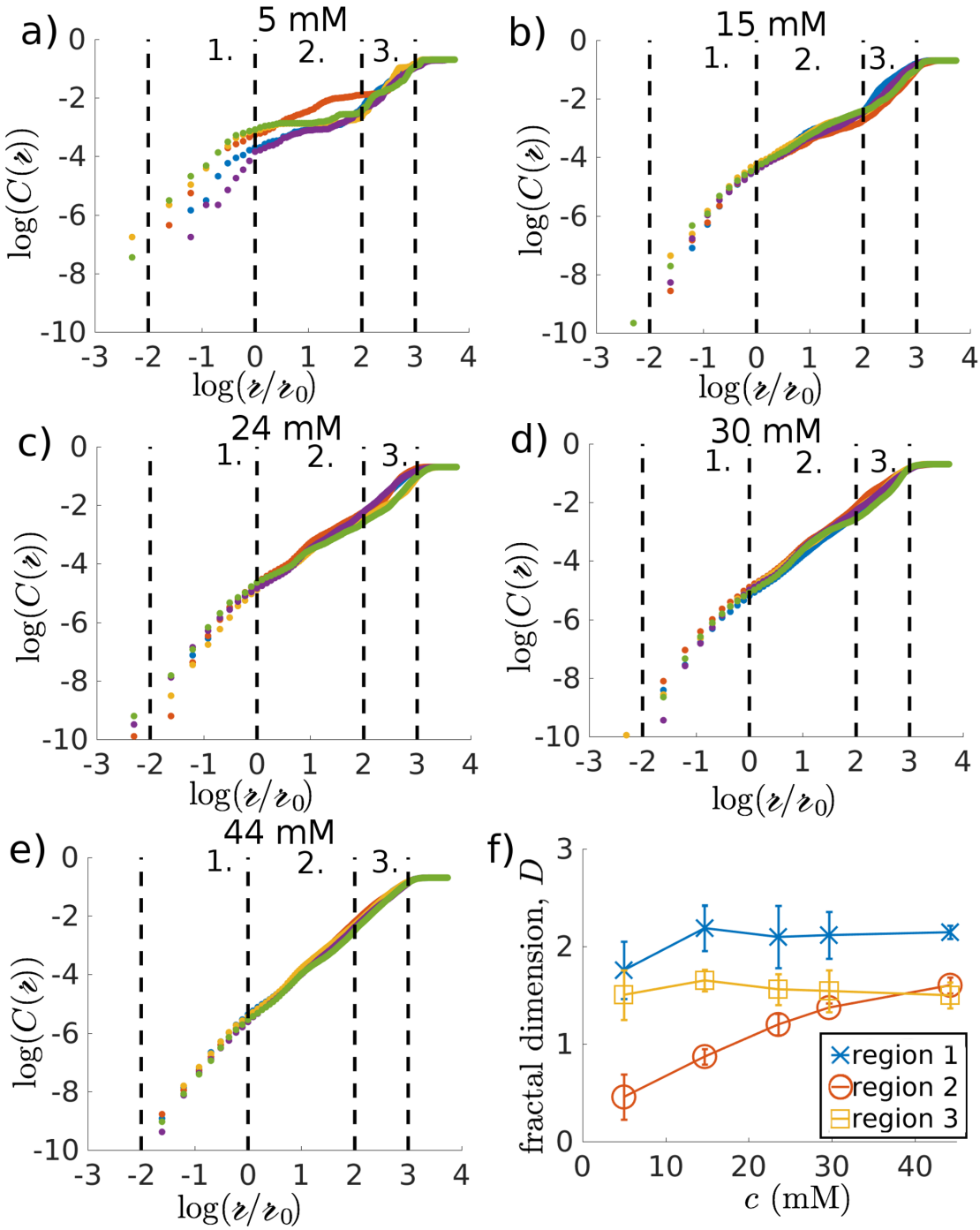

Figure 7: Fractal dimension of the hierarchical aggregates as a function of length scale. (a)-(e) Log-log plots of correlation integral $C(r)$ versus radius r at each concentration. We demarcate the three regimes that emerge from this analysis by dashed black lines. We render r dimensionless before taking the logarithm by rescaling by an arbitrary reference distance of $r_0 = 1$ nm. (f) Fractal dimension D computed from linear fits to each of the three regimes as a function of concentration.

the number of molecules in the cluster and there are 29 coarse-grained beads in each molecule (cf. Fig. 1). The eigenvalues of $\mathbf{S}$ correspond to the squared ordered principal moments of the cluster $\{\xi_i(r)\}_{i=1}^3$ that characterize its extent along its principal axes furnished by the corresponding eigenvectors[70]. The principal moments are related to the radius of gyration as $R_g = \sqrt{\xi_1^2 + \xi_2^2 + \xi_3^2}$[70]. In performing these calculations, we eliminate any potentially spurious effects introduced by the periodic walls by excising the cluster from the simulation box and unwrapping the periodic boundary conditions prior to computation of the gyration tensor. This procedure will fail for formally infinite aggregates that span the fundamental simulation cell, but we did not observe any such clusters at the concentrations studied in this work.

We plot in Fig. 8a the ensemble averaged radii of gyration $\langle R_g(r)\rangle$ and principal moments of the gyration tensor $\{\langle\xi_i(r)\rangle\}_{i=1}^3$ as a function of cluster size r averaged over all clusters observed in our simulations. As expected, $\langle R_g(r)\rangle$ and $\{\langle\xi_i(r)\rangle\}_{i=1}^3$ all trend upwards with increasing r. We plot in Fig. 8b the ensemble averaged ratios of the principal moments, $\{\langle\xi_i/\xi_j\rangle\}_{j>i}$. Ratios close to unity characterize isotropic aggregates, whereas values far from unity are indicative of high aspect ratio clusters. In Fig. 8c we plot the ensemble averaged relative shape anisotropy $\langle\kappa^2(r)\rangle$ as a function of cluster size, defined as[70],

$$\kappa^2 = \frac{3}{2}\frac{\xi_1^4 + \xi_2^4 + \xi_3^4}{(\xi_1^2 + \xi_2^2 + \xi_3^2)^2} - \frac{1}{2}, \tag{13}$$

which is bounded to the range $[0, 1]$, where $\kappa^2 = 0$ indicates that the beads in the cluster are distributed with tetrahedral or higher order symmetry and $\kappa^2 = 1$ that they are arranged along a line.

The plots of $\{\langle\xi_i/\xi_j\rangle\}_{j>i}$ and $\kappa^2(r)$ again inform a division into three regimes consistent with those identified in the fractal dimension analysis in Section 3.1.3, but this time partitioned according to cluster size r rather than observation length scale: Regime I ($1 \leq r < 27$), Regime II ($27 \leq r < 97$), and Regime III ($r \geq 97$). We present representative cluster snap-

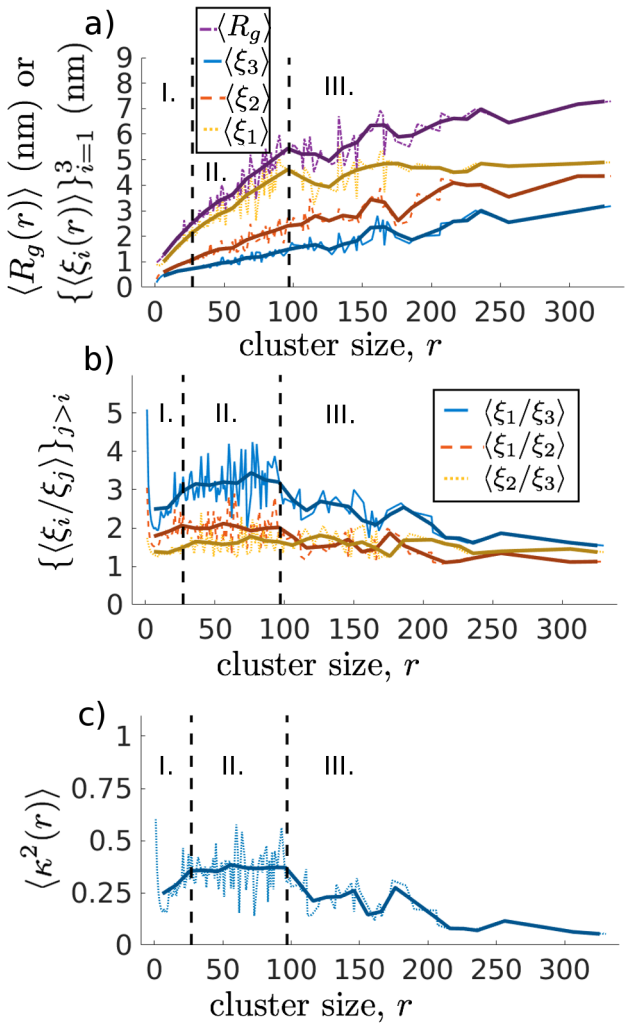

Figure 8: Gyration tensor analysis of contact clusters formed by protonated (low pH) peptides as a function of cluster size r averaged over clusters observed in our simulations at all times and concentrations. (a) Ensemble averaged radius of gyration $\langle R_g(r) \rangle$ and principal moments of the gyration tensor $\{\langle \xi_i(r) \rangle\}_{i=1}^3$. (b) Ensemble averaged ratios of the principal moments of the gyration tensor $\{\langle \xi_i/\xi_j \rangle\}_{j>i}$. (c) Ensemble averaged relative shape anisotropy $\langle \kappa^2(r) \rangle$. The thin lines correspond to mean values computed over all clusters observed in our simulations at all concentrations, and heavy lines to sliding window smoothing of the data using a window size of 10 to more clearly show the gross trends in the data. The three aggregation regimes – Regime I ($1 \leq r < 27$), Regime II ($27 \leq r < 97$), and Regime III ($r \geq 97$) – are indicated by dashed vertical lines.

shots from each regime in Fig. 9. In Regime I ($1 \leq r < 27$), we observe an initially rapid decrease in all three principal moment ratios and a concomitant decrease in the relative shape anisotropy $\langle \kappa^2(r) \rangle$ from 0.6 to 0.2 over the cluster size range $1 \leq r < 6$. This is

followed by recovery of $\langle\kappa^2(r)\rangle$ from 0.2 to 0.4 and $\langle\xi_1(r)/\xi_3(r)\rangle$ from 2 to 3 over the range $6 \leq r < 27$, while $\langle\xi_1(r)/\xi_2(r)\rangle$ and $\langle\xi_2(r)/\xi_3(r)\rangle$ remain approximately flat at 2 and 1.5, respectively. Structurally, this corresponds to the aggregation of elongated high aspect ratio monomers into more spherical optical clusters comprising several monomers, followed by the aggregation of these spherical clusters into more elongated, ellipsoidal optical and contact clusters (cf. Fig. 9a). In Regime II ($27 \leq r < 97$), the three principal moment ratios and relative shape anisotropy remain approximately constant. At these sizes the clusters no longer aggregate in a preferential direction, but begin to isotropically branch preserving the relative aspect ratios as the cluster size increases (cf. Fig. 9b). In Regime III ($r \geq 97$, up to the maximum cluster size of $r = 330$ observed in our simulations), $\langle\xi_1(r)/\xi_3(r)\rangle$ declines from 3 to 1.5, $\langle\xi_1(r)/\xi_2(r)\rangle$ from 2 to 1, and $\langle\xi_2(r)/\xi_3(r)\rangle$ remains at 1.5, with a corresponding drop in $\langle\kappa^2(r)\rangle$ from 0.4 to 0.1. This aggregation regime corresponds to the continued formation of a large-scale self-similar branched network lacking any preferred directionality and with a fractal dimension of $\sim$1.5 (cf. Fig. 9c, Fig. 7f).

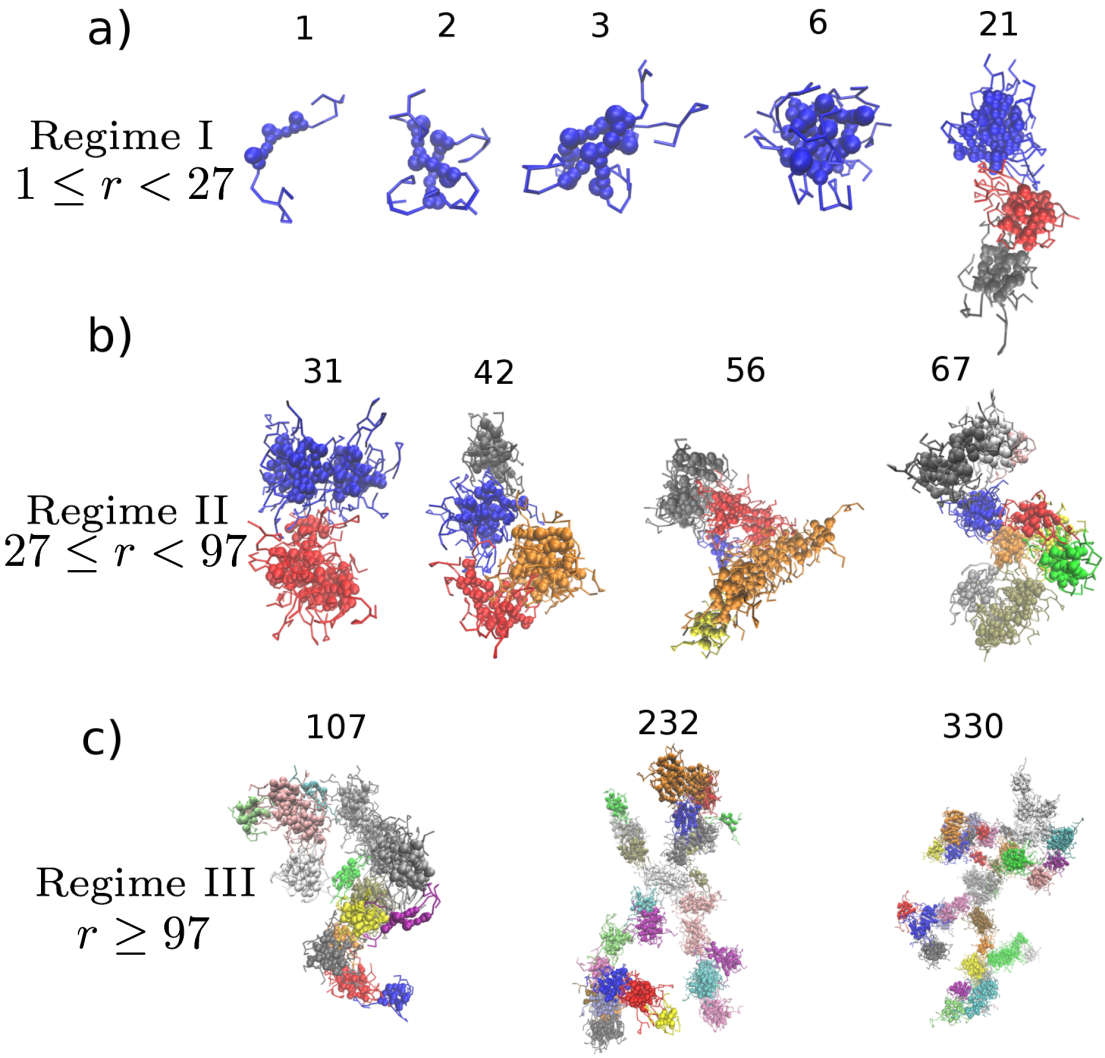

Figure 9: Representative contact clusters illustrating the hierarchical assembly process in each of the three aggregation regimes, (a) Regime I ($1 \leq r < 27$), (b) Regime II ($27 \leq r < 97$), and (c) Regime 3 ($r \geq 97$). Distinct optical clusters within the contact clusters are distinguished by different colors, and the number of monomers in each image indicated by the accompanying numeral. Each panel is scaled differently for ease of viewing the clusters of disparate sizes, but in all cases the end-to-end distance of a fully extended monomer is ∼3.5 nm and the length of each OPV3 core ∼1.5 nm.

3.2 Smoluchowski coagulation model describes the kinetics of contact cluster aggregation

Our simulations of the protonated (low pH) peptides provide information about the kinetics of hierarchical peptide self-assembly over hundreds of nanoseconds. By mining these data to parameterize a kinetic model of assembly, we can both garner insight into the microscopic assembly dynamics and extrapolate our predictions to time and length scales beyond the reach of all-atom or coarse-grained molecular simulation.

The Smoluchowski coagulation model is a general theory describing irreversible aggregation in well-mixed systems[71–73] that has been applied to a number of different systems including planetary aggregation[74,75], aerosol droplet coagulation[76], and amyloid protofibril formation[77]. This model assumes that aggregation is irreversible (i.e., fragmentation is forbidden), that the state of the system is fully specified by the cluster size distribution without differentiating clusters with regards to their particular morphologies, and that the system can be described as well mixed so that clusters need not be spatially resolved.

We propose that the Smoluchowski coagulation model can provide a quantitative description of DFAG-OPV3-GAFD contact cluster aggregation kinetics. It is an appropriate model for this process for several reasons. First, we observe aggregation of these oligopeptides at low pH conditions to be effectively irreversible over several hundred nanoseconds (cf. Fig. 5), making explicit treatment of fragmentation unnecessary. Second, we do not observe any lag phase in either simulation or experiment[17,19,20] suggesting that aggregation proceeds downhill in free energy and that nucleation-dependent models are unlikely to provide a good description[78]. Third, although we have previously used Markov state models to treat the short-time aggregation dynamics[20], Smoluchowski coagulation offers a more physically motivated model that can be straightforwardly extrapolated to longer length and time scales. Fourth, we initialize our systems as dispersed monomers meaning that the well-mixed assumption is expected to be a good description over the time scales of our simulations, and

is consistent with the absence of observed spatial gradients in experiment[17]. Fifth, any dependence of the aggregation kinetics of the observed morphological changes in the growing clusters can, if necessary, be straightforwardly captured within the Smoluchowski model as a cluster size dependent rate constant.

3.2.1. Smoluchowski coagulation model

The continuous time Smoluchowski coagulation equation for systems admitting discrete aggregate sizes is[73],

$$\frac{dn_r}{dt} = \frac{1}{2}\sum_{i=1}^{r-1} K_{i,r-i} n_i(t) n_{r-i}(t) - \sum_{i=1}^{\infty} K_{r,i} n_r(t) n_i(t), \tag{14}$$

where t is time, $K_{i,j}$ is a kernel corresponding to a second order rate constant for coagulation between aggregates of size i and size j, and $n_r(t)$ is the number concentration of aggregates of size r at time t. Analytical expressions for $n_r(t)$ are unavailable for arbitrary kernels, but solutions are known for the special cases of (i) constant $K_{ij} = K$[73,79], (ii) additive $K_{ij} = K(i+j)$[79], and (iii) multiplicative $K_{ij} = K(i)K(j)$ kernels[80]. For the homogeneous kernel $K_{ai,aj} = a^{\lambda} K_{i,j}$, expressions for $n_r(t)$ are not known, but the moments and their ratios, such as the number-averaged and mass-averaged cluster sizes, are available[72,77].

As we demonstrate below, the simplest assumption of a constant kernel $K_{ij} = K$, corresponding to size independent coagulation rate constants, provides good fits to our simulation data. Under this assumption the solution for $n_r(t)$ with arbitrary initial conditions is[79],

$$n_r(t) = 4\frac{n_r(0)}{(KtM_0(0)+2)^2} + \left(\frac{KtM_0(0)}{KtM_0(0)+2}\right)\sum_{j=1}^{r-1}\frac{n_{r-j}(0)n_j(t)}{M_0(0)}, \tag{15}$$

where $n_r(0)$ is the initial number concentration of r-mers and $M_i(t) = \sum_{r=1}^{\infty} r^i n_r(t)$ is the ith moment of the cluster size distribution at time t so that $M_0(0) = \sum_{r=1}^{\infty} n_r(0)$ is the sum of the initial number concentrations of all r-mers. For monodisperse initial conditions this

simplifies to[73,79],

$$n_r(t) = 4\frac{M_1}{(KtM_1+2)^2}\left(\frac{KM_1t}{KM_1t+2}\right)^{r-1}, \tag{16}$$

where $M_1(t) = \sum_{r=1}^{\infty} rn_r(t) = M_1(0) = M_1$ is the total concentration of monomers in solution, and is related to the concentration through Avogadro's number as $c(t) = M_1(t)/N_A$. The number-averaged cluster size $\mu_1(t)$ under arbitrary initial conditions is[73,79],

$$\mu_1(t) = \frac{M_1(t)}{M_0(t)} = \mu_1(0) + \frac{1}{2}KM_1t, \tag{17}$$

and the mass-averaged cluster size $\mu_2(t)$ under arbitrary initial conditions is[73,77,79],

$$\mu_2(t) = \frac{M_2(t)}{M_1(t)} = \mu_2(0) + KM_1t, \tag{18}$$

and following Modler et al.[77] we identify,

$$t_c = \frac{2}{KM_1}, \tag{19}$$

as a characteristic coagulation time scale, where it is conventional to retain the factor of 2 in the numerator.

3.2.2. Understanding the success of the constant Smoluchowski kernel

Assuming the constant kernel to be of the form $K_{i,j} = K = \alpha k_s$, we follow Modler et al.[77] to decompose the coagulation rate constants into the product of the sticking probability α, accounting for the probability of a productive collision, and an intrinsic rate constant k_s. Assuming diffusion controlled aggregation, we can develop an approximate expression for the intrinsic rate constant by inserting the Stokes-Einstein relation for the diffusivity of a spherical particle of radius R through a low Reynolds number liquid,

$$D = \frac{k_BT}{6\pi\eta R} \tag{20}$$

into the analytical expression for the rate constant for the collision of two Brownian hard spheres of size R_1 and R_2,

$$k_s = 4\pi(R_1 + R_2)(D_1 + D_2), \tag{21}$$

to yield[77,81,82],

$$k_s = \frac{2k_BT}{3\eta}\left(2 + \frac{R_1}{R_2} + \frac{R_2}{R_1}\right), \tag{22}$$

where T is the temperature, k_B is Boltzmann's constant, and η is the solvent viscosity. Eqn. 22 provides a means to understand the success of the constant kernel in recapitulating our simulation data. First, we showed in Section 3.1.3 that contact clusters are fractal objects of dimensionality $D \approx 1.5$, meaning that their characteristic radius R scales weakly with cluster size r as $R \sim r^{2/3}$. Second, although the time resolved contact cluster size distributions in Fig. 4b are relatively broad, they span no more than an order of magnitude over the course of our simulation, meaning that at any time instant we are unlikely to observe collisions between clusters of vastly discrepant sizes. Accordingly, the terms $\frac{R_i}{R_j} \sim \left(\frac{r_i}{r_j}\right)^{2/3}$ are both expected to be of order unity, leading us to predict an approximately size-independent intrinsic rate constant,

$$k_s \approx \frac{8k_BT}{3\eta}. \tag{23}$$

Assuming that the sticking probability α is not a strong function of cluster size, this analysis provides a theoretical rationalization for the use of a size-independent Smoluchowski coagulation kernel $K_{i,j} = K = \alpha k_s$. Modler et al.[77] have previously demonstrated the validity of this assumption in the context of amyloid peptides by showing good agreement between numerical solutions employing size-dependent and size-independent intrinsic rate constants.

3.2.3. Inference of Smoluchowski coagulation rate constant

We now analyze our coarse-grained molecular simulation trajectories to determine the best fit constant kernel K for the Smoluchowski coagulation model. Appealing to Eqn. 18, we plot the mass-averaged contact cluster size measured in our simulations as a function of time

$\mu_2(t)$ and compute the least squares linear fit, from which we estimate K by dividing the slope by the total monomer concentration M_1. The linear fits at each concentration are presented in Fig. 10 and the best fit values of K presented in Table 1.

Table 1: Coagulation rate constant K as a function of concentration, estimated from least squares linear fits of the measured mass-averaged contact cluster size $\mu_2(t)$ using Eqn. 18. Uncertainties are estimated from the standard deviation σ_K in K computed over the five independent production runs.

Concentration, c (mM)	K (ns^{-1} nm^3)
5.0	6 ± 1
15	5.9 ± 0.8
24	9 ± 3
30	8 ± 1
44	17 ± 7

Inserting the best fit coagulation rate constant into the analytical Smoluchowski expressions for $n_r(t)$ (Eqn. 15) shows good agreement with the number concentration time courses measured in simulation. We present in Fig. 11, a comparison of the simulation results and analytical expressions for the number concentrations from monomers to 12-mers in the 24 mM system and provide analogous plots for the other concentrations in Figs. S6-S9. The agreement for larger aggregates deteriorates somewhat due to both a paucity of simulation data for large aggregate sizes due to the relative rarity of large aggregates, and finite size effects wherein the finite number of monomers in the simulations stands in contrast to the assumption of the Smoluchowski model of an infinite system and monomer supply (Fig. S10). Nevertheless, that this simple spatially-unresolved model assuming size-invariant coagulation rate constants is capable of quantitatively recapitulating the number fraction time courses of the small to medium-sized clusters for which we have good simulation data supports the Smoluchowski coagulation model as a good description of the aggregation kinetics.

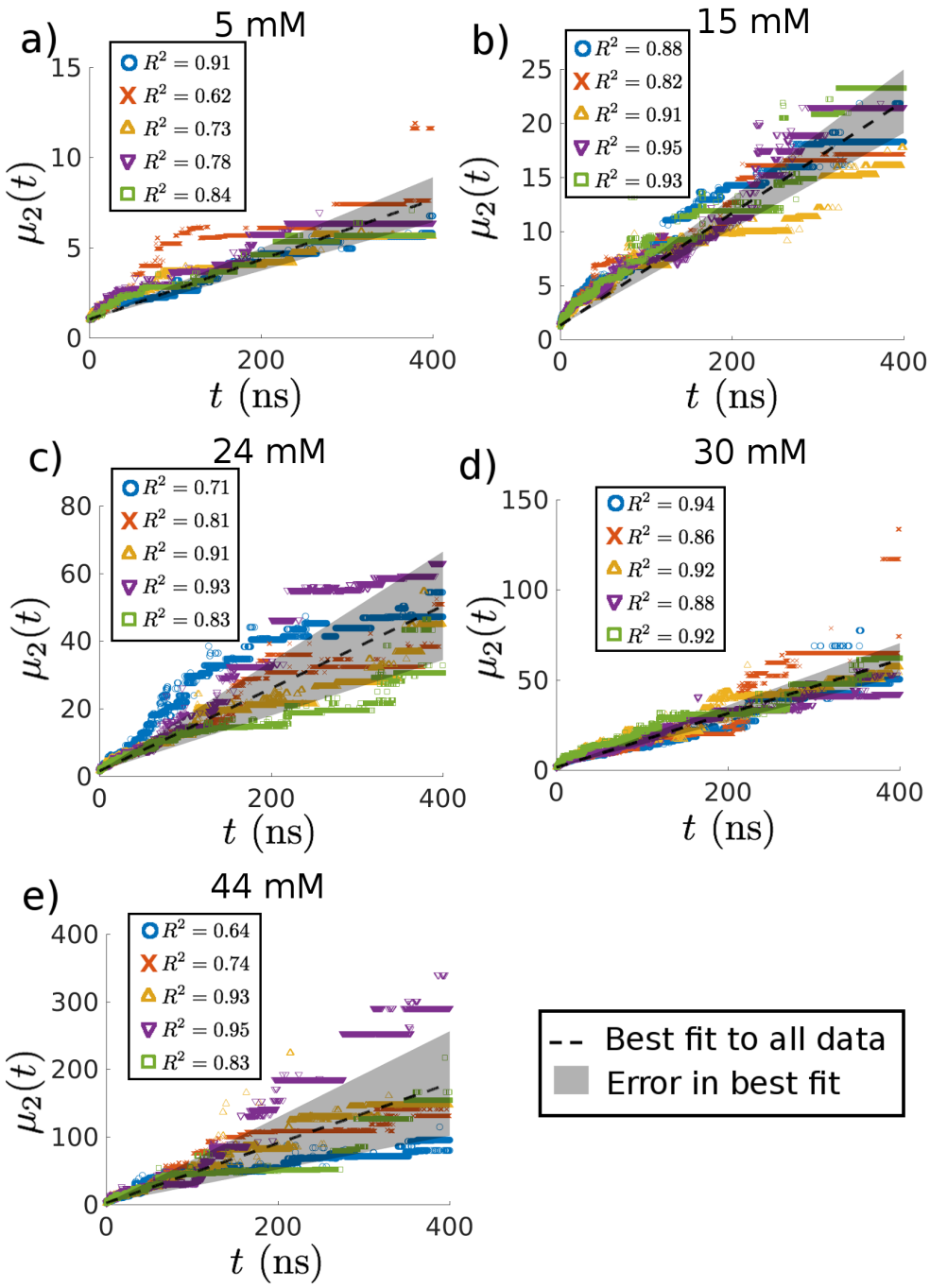

Figure 10: Mass-averaged cluster size as a function of time $\mu_2(t)$ measured in simulations at concentrations (a) 5.0 mM, (b) 15 mM, (c) 24 mM, (d) 30 mM, and (e) 44 mM. Black lines indicate the least squares linear fits to all five independent runs. The shaded area indicates the uncertainty in the best fit computed from the standard deviation in the slopes computed for each individual run. Data from each independent simulation are presented in different colors using different symbols, and are labeled with the R^2 value of the best fit line.

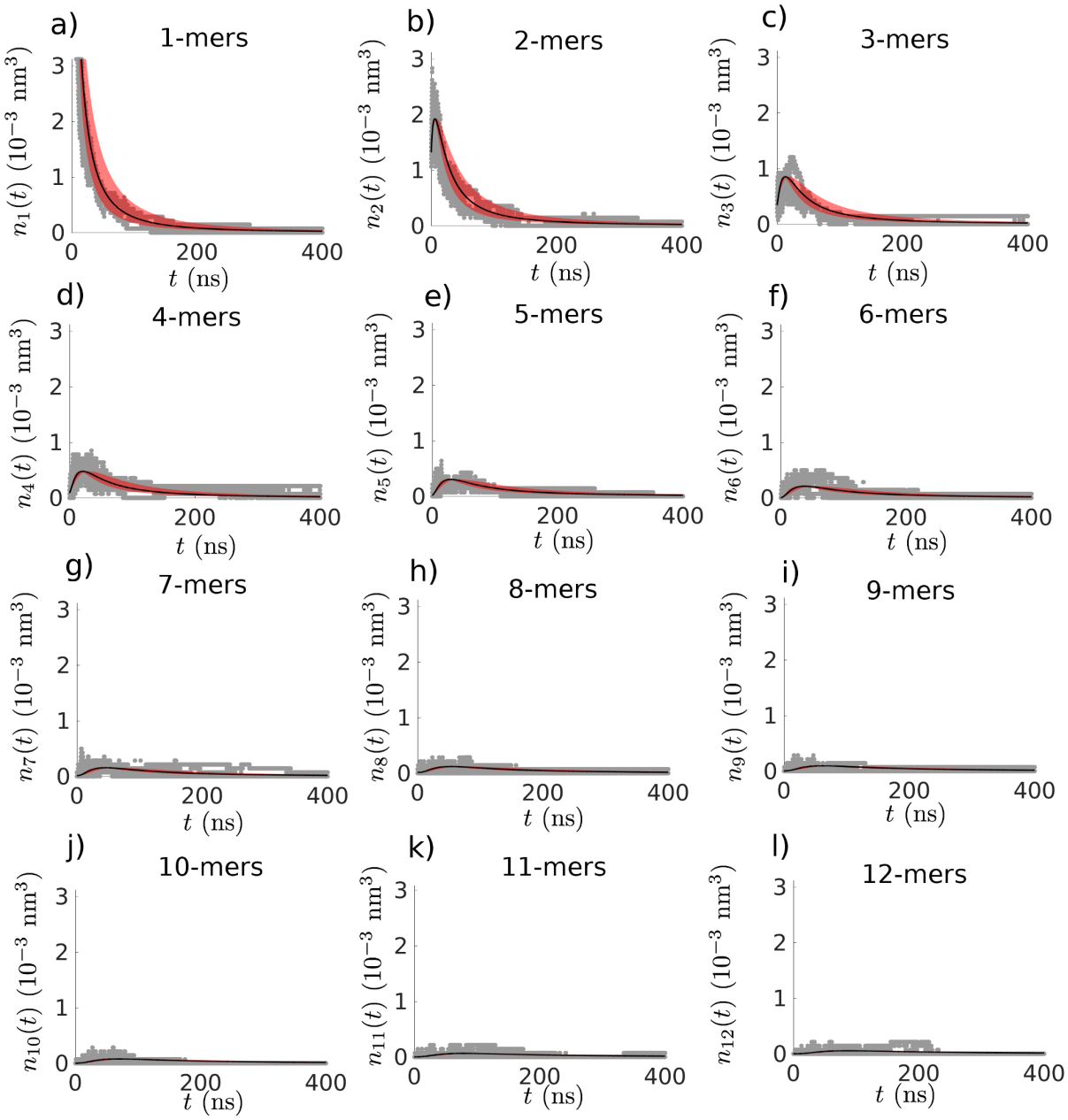

Figure 11: Comparison of time evolution of cluster number concentrations observed in simulation with those predicted by the fitted Smoluchowski coagulation equation for the aggregation of protonated (low pH) peptides at 24 mM. Number concentration time courses for (a-l) monomers through 12-mers. Simulation data are displayed in gray for the five separate runs. The analytical predictions of the Smoluchowski coagulation model employing the best fit value of $K = 9$ ns^{-1} nm^3 (Table 1) are presented as a dashed black line. Red shading illustrates the sensitivity of the model predictions to K over the range $K \pm \sigma_K$, where σ_K is the standard deviation of K computed over the five independent production runs. Analogous plots for the four other concentrations studied are presented in Figs. S6-S9.

3.2.4. The characteristic coagulation time has a simple concentration dependence

The characteristic coagulation time is inversely proportional to both the coagulation rate constant and the monomer concentration, $t_c = \frac{2}{KM_1} = \frac{2}{KcN_A}$ (Eqn. 19). Employing the best fit values of K in Table 1, the plot of t_c as a function of c in Fig. 12 reveals an approximate power law dependence of the form,

$$\log\left(t_c/t_c^0\right) = -\gamma \log\left(c/c^0\right) + \log\left(\zeta\right), \tag{24}$$

where $t_c^0 = 1$ ns and $c^0 = 1$ mM are an arbitrary reference time scale and concentration to make dimensionless the arguments of the logarithm. Linear least squares regression in which we handled the observed heteroskedasticity in the data by weighting each data point in inverse proportion to its variance[83] reveal best fit parameters of $\gamma = 1.3$ (95% CI: 0.9, 1.7) and $\zeta = 1000$ (95% CI: 400, 3000). A concentration invariant coagulation rate constant would produce a simple $t_c \propto c^{-1}$ dependence, and the observed deviation from this scaling reflects the concentration dependence of K (Table 1).

At peptide concentrations of 0.86 mM (0.1 mg/mL) realized in the directed assembly of peptide oligomers in microfluidic devices[19], our best fit parameters predict a coagulation time $t_c = 800$ ns (95% CI: 200 ns, 1400 ns), in good agreement within error bars of the 2500 ns (95% CI: 500 ns, 9300 ns) characteristic assembly time scale previously predicted under these conditions by Thurston et al.[20] using Markov state models fitted to all-atom implicit solvent calculations.

Finally, we observe the powerful interpretation of Fig. 12 as a calibration curve relating the concentration c as a macroscopic experimental control parameter to the microscopic characteristic coagulation time t_c. This relationship can be used to infer, for a particular concentration, the characteristic coagulation time t_c and therefore the microscopic Smoluchowski model coagulation rate constant through $K = \frac{2}{t_c c N_A}$. The estimate of K provides

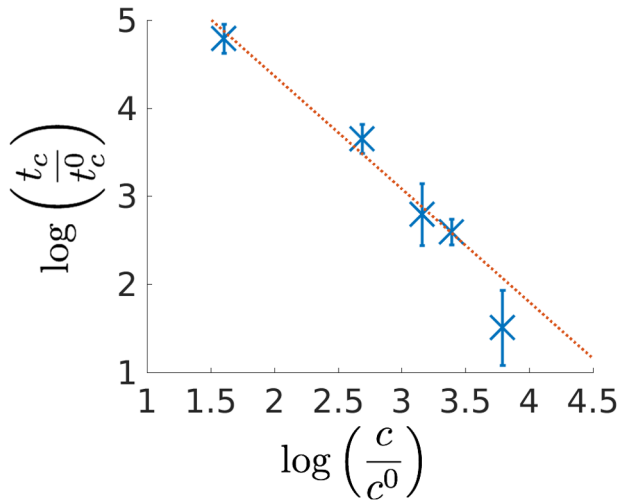

Figure 12: Log-log plot of coagulation time t_c as a function of initial monomer concentration. The dotted red line represents a least squares fit of a power law form $t_c(c) = \zeta c^{-\gamma}$ where each data point is weighted in inverse proportion to its variance, from which we estimate $\gamma = 1.3$ (95% CI: 0.9, 1.7) and $\zeta = 1000$ (95% CI: 400, 3000). We render t_c and c dimensionless prior to taking logarithms by rescaling by the arbitrary reference time $t_c^0 = 1$ ns and concentration $c^0 = 1$ mM.

access to predictions of the microscopic temporal evolution of each cluster size $n_r(t)$ and moments of the cluster size distribution through the analytical solutions in Eqns. 15-19.

3.2.5. Cluster size evolutions exhibit approximate scaling collapse

Under a homogeneous coagulation kernel $K_{ai,aj} = a^\lambda K_{i,j}$ – of which the constant kernel is a special case with $\lambda = 0$ – the Smoluchowski model predicts that if $n_r(t)$ is a solution to Eqn. 14, then so is $\frac{a^{\lambda+1}}{b} n_{ar}(bt)$. This self-similarity leads to the prediction of a scaling form of the solution valid for long times and large cluster sizes[72,73,76,84],

$$n_r(t) \sim s(t)^{-2}\phi(r/s(t)), \tag{25}$$

where $\phi(x)$ is a master function that will be the same for all $n_r(t)$, and $s(t)$ is the ratio of any two consecutive moments of the cluster size distribution[76],

$$s(t) = \frac{M_i(t)}{M_{i-1}(t)}. \tag{26}$$

This "scaling hypothesis" states that for long times and large cluster sizes, all number concentrations will evolve to a self-similar distribution of the form of Eqn. 25, regardless of the precise initial conditions, as long as those initial conditions are sufficiently narrow (i.e., not power-law-distributed). Although the hypothesis remains unproven for arbitrary kernels and initial conditions, it has been supported by substantial numerical evidence and is proven for the particular case of a constant kernel with monodisperse initial conditions of interest here[72,73,76,85].

Adopting $s(t) = \frac{M_2(t)}{M_1(t)} = \mu_2(t)$, if Smoluchowski coagulation serves as a good model for peptide aggregation, we should expect to see scaling collapse in our data of the form,

$$n_r(t)\mu_2(t)^2 \sim \phi(r/\mu_2(t)). \tag{27}$$

We plot in Fig. 13 $n_r(t)\mu_2(t)^2$ against $(r/\mu_2(t))$ for all contact clusters of size greater than 20 at each concentration, and in Fig. 14 for contact clusters of size 1, 3, 5, 11, 20, and 30 aggregated over all concentrations studied. We exclude clusters smaller than size 20 in Fig. 13 since – as evinced in Fig. 14a-d – the scaling relation is not predicted to hold for small clusters and/or early times. In testing the scaling hypothesis for our simulation data, there is an inherent trade-off between analyzing small cluster sizes where we possess many observations and analyzing large cluster sizes where the scaling relation is expected to be most valid. Due to a relative paucity of observational data for cluster sizes in excess of ∼50, we restrict our analysis in Fig. 14 to clusters of a maximum size of 30. That we observe approximate data collapse onto a master curve $\phi(r/\mu_2(t))$ for sufficiently large clusters for which we possess sufficient statistics provides further support for the validity

of the Smoluchowski coagulation model and self-similarity in the aggregation dynamics at multiple concentrations. There are two key implications of this result. First, the initial conditions do not strongly affect the long-time dynamics of assembly. In particular, the cluster size distributions at long times ($t \gg t_c$) do not depend on whether the initial system is comprised of monodisperse monomers as employed in our simulations, or a distribution of oligomers as a more realistic description of the high-pH aggregation state of the system (cf. Fig. 4a). Second, the aggregation mechanism does not change as a function of concentration. Monomer concentration affects the rate of aggregation (cf. Fig. 12), but not its underlying mechanism over the 5-44 mM concentration range studied in this work.

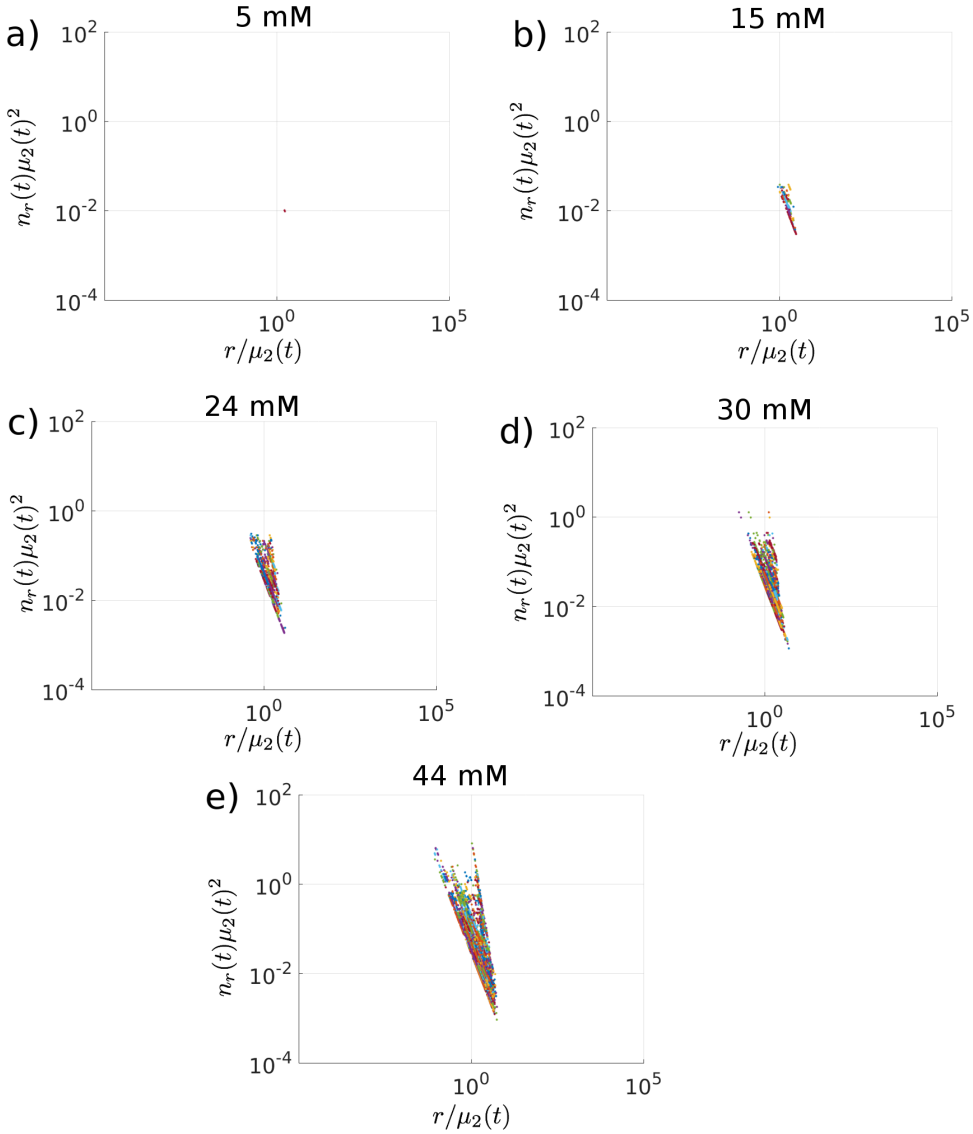

Figure 13: Plot of $n_r(t)\mu_2(t)^2$ against $r/\mu_2(t)$ at concentrations (a) 5.0 mM, (b) 15 mM, (c) 24 mM, (d) 30 mM, and (e) 44 mM. Data are presented for clusters of size 20 and larger where the long-time scaling relation Eqn. 27 approximately holds. We observe approximate data collapse onto a master curve $\phi(r/\mu_2(t))$. The visually apparent diagonal "streaking" occurs due to the discrete nature of cluster sizes.

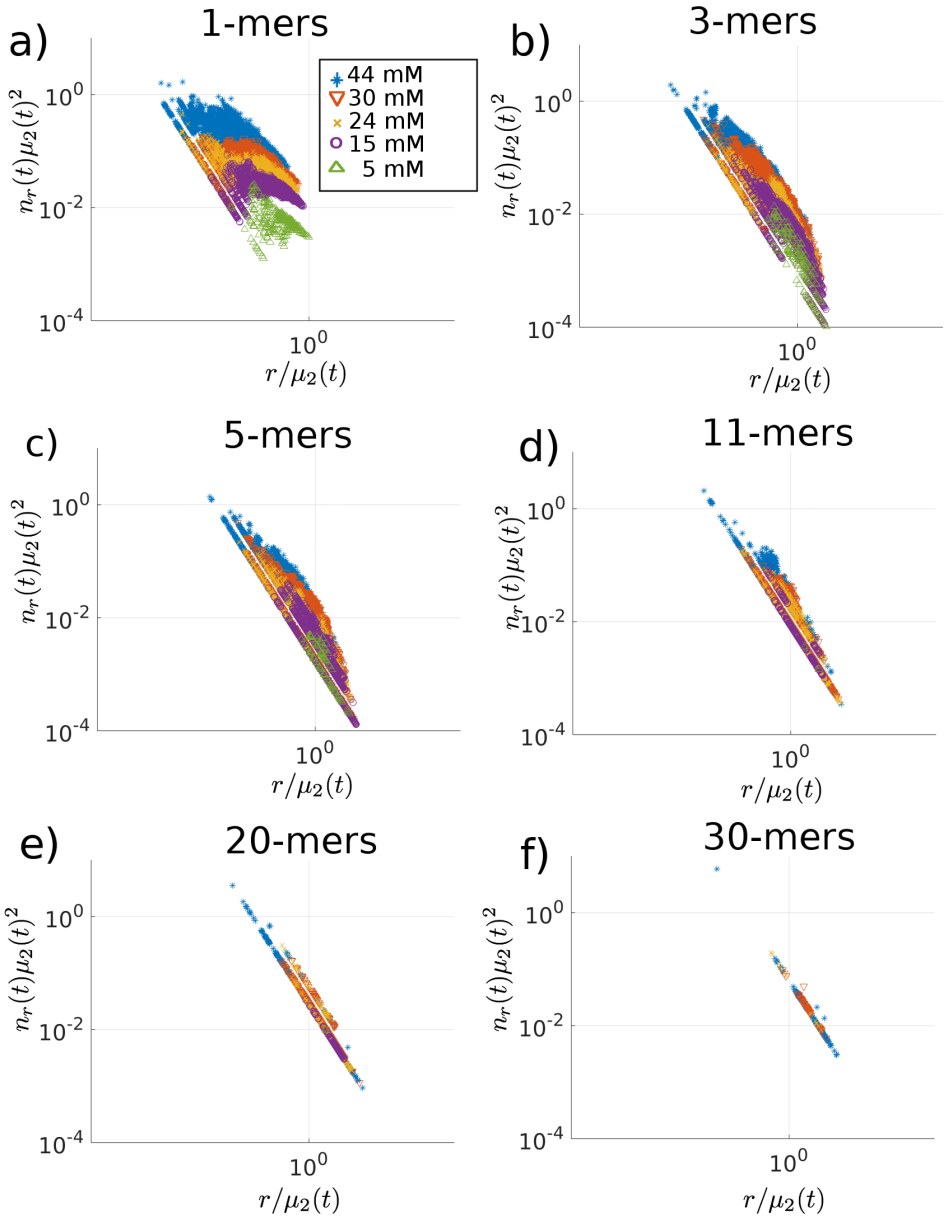

Figure 14: Plot of $n_r(t)\mu_2(t)^2$ against $r/\mu_2(t)$ for clusters observed in simulations at all concentrations studied of size (a) 1, (b) 3, (c) 5, (d) 11, (e) 20, and (f) 30. We observe approximate data collapse onto a master curve $\phi(r/\mu_2(t))$, where the long-time scaling relation Eqn. 27 serves as a better approximation for larger clusters formed at later times. The visually apparent diagonal "streaking" occurs due to the discrete nature of cluster sizes.

3.3 Analytical predictions of Smoluchowski model

Assuming that underlying mechanisms of assembly remain unchanged for larger cluster sizes, we may extrapolate our Smoluchowski coagulation equation fitted for the aggregation of hundreds of peptides over hundreds of nanoseconds to make predictions of assembly at longer time and length scales. It is conceivable that additional physical concerns come into play for sufficiently large cluster sizes that qualitatively change the structure and dynamics of assembly, but in the absence of data in very large cluster size regimes we quantify the uncertainties in our extrapolation based on the uncertainty in the coagulation rate constant K estimated from the least squares fit of the concentration dependent characteristic coagulation time (Fig. 12). In Fig. 15, we present the analytical Smoluchowski predictions for the time evolution of clusters of size $r = 10^2$ ($\sim$10 nm), 10^3 ($\sim$100 nm), 10^4 ($\sim$1000 nm), 10^5 ($\sim$10,000 nm), and 10^6 ($\sim$100,000 nm) using the analytical solutions for $n_r(t)$ in Eqn. 16 at a concentration of $c = 0.86$ mM (0.1 mg/mL, $M_1 = 5 \times 10^{-4}$ nm^{-3}) previously employed in the directed microfluidic assembly of DFAG-OPV3-GAFD peptides[19] and a value of $K = 5$ ns^{-1} nm^3 (95% CI: 3 ns^{-1} nm^3, 7 ns^{-1} nm^3) estimated from the concentration dependent extrapolation in Fig. 12. Estimates of the approximate linear dimension of each cluster size were made from simple extrapolations of the observation that clusters of $\sim$100 monomers in our simulations possess typical linear dimensions of $\sim$10 nm. The confidence intervals in K were estimated by resampling the t_c values plotted in Fig. 12 from Gaussians with variances matched to the standard deviations in the data and recomputing the least squares fit from which the value of K at 0.86 mM was extrapolated over 100 rounds of this bootstrap resampling procedure.

The curves in Fig. 15 represent theoretical predictions of the dynamical evolution of selected cluster sizes from our extrapolated Smoluchowski coagulation model, all of which collapse to the same curve, as expected from the scaling hypothesis that holds at long times and large cluster sizes[73]. Since it is extremely challenging to experimentally track the dy-

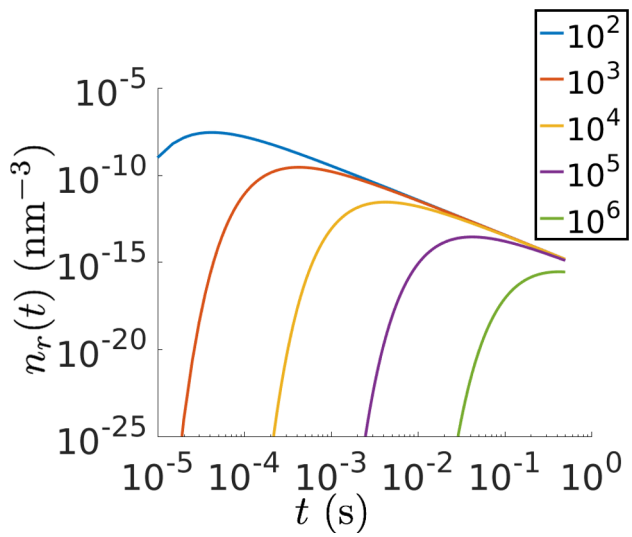

Figure 15: Analytical Smoluchowski predictions using Eqn. 16 of the number concentrations $n_r(t)$ of aggregates of sizes $r = 10^2$, $r = 10^3$, $r = 10^4$, $r = 10^5$, and $r = 10^6$ versus time t at a concentration of $c = 0.86$ mM (0.1 mg/mL, $M_1 = 5 \times 10^{-4}$ nm^{-3}). The solutions converge at long times in line with the predictions of the scaling hypothesis[73].

namics of particular cluster sizes, we cannot compare these predictions directly to experiment but can make experimental contact on a coarser level through the mass-averaged cluster size. In the directed assembly of aligned DFAG-OPV3-GAFD aggregates in a microfluidic flow cell at $c = 0.86$ mM (0.1 mg/mL), Marciel et al.[19] reported the assembly and fluorescent detection of assemblies of diameter $\sim$10 μm on time scales of $\sim$10 s. Using the same approximate conversion between cluster size and linear dimension as described above, these clusters are expected to contain $O(10^5)$ monomers. Rearranging the analytical expression for the mass-averaged cluster size in Eqn. 18, we can estimate the time required for the coagulation process to produce a particular mass-averaged cluster size as,

$$t(c) = \frac{(\mu_2 - \mu_2(0))}{KM_1} = \frac{t_c(c)}{2}(\mu_2 - \mu_2(0)), \tag{28}$$

where $t_c(c{=}0.86 \text{ mM}) = 800$ ns ($K(c{=}0.86 \text{ mM}) = 5$ ns^{-1} nm^3) is extracted from the least squares fit in Fig. 12, and $\mu_2(0)$ is the initial mass-averaged cluster size. The experiments of Marciel et al.[19] triggered assembly by combining an initially high pH stream containing the peptides with a low pH acid stream to drop the pH and trigger assembly. We ap-

proximately replicate this initial state by estimating $\mu_2(0) = (3.08 \pm 0.03)$ from the final hundred nanoseconds of the equilibrated deprotonated simulation to represent the high pH aggregation state.

Solving Eqn. 28 with $\mu_2 = 10^5$, $\mu_2(0) = 3.08$, and $t_c(c{=}0.86\ \text{mM}) = 800$ ns, we predict that the time required for the spontaneous assembly of aggregates of this size to be 40 ms (95% CI: 10 ms, 70 ms). Our estimate is three orders of magnitude slower than that reported by Marciel et al.[19], suggesting that there are slow dynamical processes occurring in the flow cell that are not captured within our Smoluchowski coagulation model. We hypothesize that these slow processes correspond to flow induced ripening of the contact clusters through internal rearrangements to form larger and better ordered optical clusters with π-π stacking of the OPV3 cores to form assemblies possessing fluorescent responses (cf. Fig. 5). Contact clusters lacking this alignment are not expected to strongly fluoresce, suggesting that aggregation and fluorescence are not coextensive and that alternative experiential techniques would be required to detect contact cluster formation as a distinct process from optical cluster formation. Furthermore, the experimentally reported morphologies of the aligned aggregates under the extensional flow field employed in the microfluidic cell and under quiescent conditions are known to possess significant structural differences[19], indicating an important coupling of flow to the mechanisms and dynamics of assembly on large length scales. Together, these findings suggest a need for additional computational work to make better contact with experimental work by employing electronic structure calculations to probe the different fluorescent properties of contact and optical clusters, and more highly coarse-grained mesoscale models capable of probing the effect of flow on peptide assembly at longer time and length scales.

4. CONCLUSIONS

We have presented a computational study to probe the molecular details of the early-stage self-assembly of Asp-Phe-Ala-Gly-OPV3-Gly-Ala-Phe-Asp (DFAG-OPV3-GAFD) monomers

containing an OPV3 (distyrylbenzene) core as a π-conjugated biocompatible oligopeptide that undergoes pH-triggered self-assembly into β-sheet-like nanostructures with experimentally-observed optoelectronic functionality. We developed a coarse-grained molecular model for this system explicitly parameterized against all-atom calculations that recapitulates the configurational statistics of the intramolecular bonded interactions, intra-peptide contact maps, and potentials of mean force for peptide collapse and dimerization observed in atomistic calculations. This protocol can be straightforwardly extended to develop coarse-grained models of other π-conjugated molecules with different peptide and core chemistries.

Using our computationally efficient coarse-grained model, we conducted molecular dynamics simulations of the assembly of hundreds of peptides over hundreds of nanoseconds. Morphological characterization shows the initial stages of assembly proceed hierarchically. Monomers first form oligomers of ≤ 8 peptides with aligned aromatic cores (aligned clusters), which subsequently assemble into larger aggregates of $\lesssim$40 peptides exhibiting strong associations between the π-conjugated cores (optical clusters). Optical clusters associate irreversibly via side chain interactions to form large relatively disordered aggregates that we refer to as contact clusters. Contact clusters initially form into elongated ellipses with fractal dimension $D \approx 1.5$, which begin to display branching behavior at peptide numbers of $\sim$50-100. Internal rearrangements with these contact clusters produce increasingly large optical clusters, but at a far slower rate than that of the formation of the contact clusters themselves. Experimental work has shown the importance of flow in ordering the self-assembled peptide aggregates on large length scales[17,19]. Our molecular simulations suggest a role for flow in suppressing branching behavior and network formation to rotationally align the contact clusters into linear fibrillar bundles with improved π-π stacking and optoelectronic properties.

Kinetically, we have shown aggregation of contact clusters to be well described by a Smoluchowki coagulation model as a predictive phenomenological model of non-equilibrium assembly[73]. Assuming a size-independent coagulation rate constant, we estimated this single

fitting parameter from our molecular simulation data to establish analytical expressions for the time evolution of arbitrary cluster sizes and moments of the cluster size distribution. We demonstrated using the predicted scaling behavior of the Smoluchowski model that the aggregation dynamics observed in our simulations are self-similar, indicating that the long-time assembly behavior depends only weakly on initial conditions and the assembly mechanism does not change with concentration over the 5-44 mM range studied in this work. Furthermore, we established a calibration curve to permit estimation of the coagulation rate constant as a function of concentration, permitting the inexpensive analytical prediction of the microscopic cluster size evolution using the analytical predictions of the Smoluchowski model without the need to conduct any additional molecular simulations.

By revealing the molecular details of the hierarchical assembly mechanism over hundreds of nanoseconds and developing a phenomenological coagulation model of non-equilibrium assembly kinetics, our work provides new fundamental understanding of peptide self-assembly and a route to rationally engineer π-conjugated peptide chemistry and environmental conditions to tune the morphology, kinetics, and optoelectronic properties of the emergent supramolecular assemblies. In future work, we will employ our modeling protocol to develop coarse-grained models of other oligopeptide chemistries containing different peptide sequences or π-conjugated cores (e.g., DXXX-Π-XXXD, where X = {G,A,I,V,F} and Π includes oligophenylvinylenes, oligothiophenes, and rylene diimides[15,18,86]), and explicitly incorporate the effects of flow by conducting non-equilibrium molecular dynamics simulations implementing Lees-Edwards[87] or Kraynik-Reinelt[88] boundary conditions[89]. Electronic structure calculations on representative aligned, optical, and contact clusters observed in this work will be informative in ascertaining the optoelectronic properties of the aggregates at each stage of the assembly hierarchy[90–93]. We are also working to incorporate the Smoluchowski coagulation model fitted against our molecular simulation data into a multi-scale model of peptide assembly within a microfluidic flow cell to enable explicit comparisons with experimental measurements and provide a predictive model for peptide assembly as a func-

tion of peptide chemistry and the architecture and operating conditions of the microfluidic device[19].

Supporting Information Available

Figures containing bonded distributions for reparameterized coarse-grained and atomistic systems, force field parameters, and comparison of Smoluchowski predictions to simulation. Files `b0-b8.txt` and `a0-a12.txt` containing the tabulated force field files and file `topology.txt` the DFAG coarse-grained topology. This material is available free of charge via the Internet at http://pubs.acs.org/.

Acknowledgement

This work was supported by the U.S. Department of Energy, Office of Science, Basic Energy Sciences, under Award # DE-SC0011847. R.A.M. acknowledges a graduate fellowship from the Computational Science and Engineering Program at the University of Illinois. We thank Prof. Charles Schroeder, Prof. Jianjun Cheng, Dr. Bill Wilson, and Prof. Man Hoi Lee for fruitful discussions.

References

(1) Tuttle, T. Computational Approaches to Understanding the Self-assembly of Peptide-based Nanostructures. *Isr. J. Chem.* **2015**, *55*, 724–734.

(2) Mehdizadeh, H.; Somo, S. I.; Bayrak, E. S.; Brey, E. M.; Cinar, A. Design of Polymer Scaffolds for Tissue Engineering Applications. *Ind. Eng. Chem. Res.* **2015**, *54*, 2317–2328.

(3) Subramani, K.; Ahmed, W. *Emerging Nanotechnologies in Dentistry: Processes, Materials and Applications*; William Andrew: Waltham, USA, 2011.

(4) Hosseinkhani, H.; Hong, P.-D.; Yu, D.-S. Self-assembled Proteins and Peptides for Regenerative Medicine. *Chem. Rev. (Washington, DC, U. S.)* **2013**, *113*, 4837–4861.

(5) Palmer, L. C.; Newcomb, C. J.; Kaltz, S. R.; Spoerke, E. D.; Stupp, S. I. Biomimetic Systems for Hydroxyapatite Mineralization Inspired by Bone and Enamel. *Chem. Rev. (Washington, DC, U. S.)* **2008**, *108*, 4754–4783.

(6) Hartgerink, J. D.; Beniash, E.; Stupp, S. I. Self-assembly and Mineralization of Peptide-Amphiphile Nanofibers. *Science (Washington, DC, U. S.)* **2001**, *294*, 1684–1688.

(7) Löwik, D. W.; Leunissen, E.; Van den Heuvel, M.; Hansen, M.; van Hest, J. C. Stimulus Responsive Peptide Based Materials. *Chem. Soc. Rev.* **2010**, *39*, 3394–3412.

(8) Ulijn, R. V.; Smith, A. M. Designing Peptide Based Nanomaterials. *Chem. Soc. Rev.* **2008**, *37*, 664–675.

(9) Bull, S. R.; Guler, M. O.; Bras, R. E.; Meade, T. J.; Stupp, S. I. Self-assembled Peptide Amphiphile Nanofibers Conjugated to MRI Contrast Agents. *Nano Lett.* **2005**, *5*, 1–4.

(10) Zelzer, M.; Ulijn, R. V. Next-generation Peptide Nanomaterials: Molecular Networks, Interfaces and Supramolecular Functionality. *Chem. Soc. Rev.* **2010**, *39*, 3351–3357.

(11) Guo, X.; Baumgarten, M.; Müllen, K. Designing π-Conjugated Polymers for Organic Electronics. *Prog. Polym. Sci.* **2013**, *38*, 1832–1908.

(12) Bian, L.; Zhu, E.; Tang, J.; Tang, W.; Zhang, F. Recent Progress in the Design of Narrow Bandgap Conjugated Polymers for High-efficiency Organic Solar Cells. *Prog. Polym. Sci.* **2012**, *37*, 1292–1331.

(13) Kim, S. H.; Parquette, J. R. A Model for the Controlled Assembly of Semiconductor Peptides. *Nanoscale* **2012**, *4*, 6940–6947.

(14) Hoeben, F. J.; Jonkheijm, P.; Meijer, E.; Schenning, A. P. About Supramolecular Assemblies of π-Conjugated Systems. *Chem. Rev. (Washington, DC, U. S.)* **2005**, *105*, 1491–1546.

(15) Vadehra, G. S.; Wall, B. D.; Diegelmann, S. R.; Tovar, J. D. On-resin Dimerization Incorporates a Diverse Array of π-Conjugated Functionality within Aqueous Self-assembling Peptide Backbones. *Chem. Commun. (Cambridge, U. K.)* **2010**, *46*, 3947–3949.

(16) Wall, B. D.; Zacca, A. E.; Sanders, A. M.; Wilson, W. L.; Ferguson, A. L.; Tovar, J. D. Supramolecular Polymorphism: Tunable Electronic Interactions within π-Conjugated Peptide Nanostructures Dictated by Primary Amino Acid Sequence. *Langmuir* **2014**, *30*, 5946–5956.

(17) Wall, B. D.; Tovar, J. D. Synthesis and Characterization of π-Conjugated Peptide-based Supramolecular Materials. *Pure Appl. Chem.* **2012**, *84*, 1039–1045.

(18) Wall, B. D.; Zhou, Y.; Mei, S.; Ardoña, H. A. M.; Ferguson, A. L.; Tovar, J. D. Variation of Formal Hydrogen-Bonding Networks within Electronically Delocalized π-Conjugated Oligopeptide Nanostructures. *Langmuir* **2014**, *30*, 11375–11385.

(19) Marciel, A. B.; Tanyeri, M.; Wall, B. D.; Tovar, J. D.; Schroeder, C. M.; Wilson, W. L. Fluidic-Directed Assembly of Aligned Oligopeptides with π-Conjugated Cores. *Adv. Mater. (Weinheim, Ger.)* **2013**, *25*, 6398–6404.

(20) Thurston, B. A.; Tovar, J. D.; Ferguson, A. L. Thermodynamics, Morphology, and Kinetics of Early-stage Self-assembly of π-Conjugated Oligopeptides. *Mol. Simul.* **2016**, *42*, 1–21.

(21) Fitzpatrick, A. W. P. et al. Atomic Structure and Hierarchical Assembly of a Cross-β Amyloid Fibril. *Proc. Natl. Acad. Sci. U. S. A.* **2013**, *110*, 5468–5473.

(22) Monticelli, L.; Kandasamy, S. K.; Periole, X.; Larson, R. G.; Tieleman, D. P.; Marrink, S.-J. The MARTINI Coarse-grained Force Field: Extension to Proteins. *J. Chem. Theory Comput.* **2008**, *4*, 819–834.

(23) de Jong, D. H.; Singh, G.; Bennett, W. D.; Arnarez, C.; Wassenaar, T. A.; Schafer, L. V.; Periole, X.; Tieleman, D. P.; Marrink, S. J. Improved Parameters for the Martini Coarse-grained Protein Force Field. *J. Chem. Theory Comput.* **2012**, *9*, 687–697.

(24) Bond, P. J.; Holyoake, J.; Ivetac, A.; Khalid, S.; Sansom, M. S. Coarse-grained Molecular Dynamics Simulations of Membrane Proteins and Peptides. *J. Struct. Biol.* **2007**, *157*, 593–605.

(25) Nielsen, S. O.; Lopez, C. F.; Srinivas, G.; Klein, M. L. Coarse Grain Models and the Computer Simulation of Soft Materials. *J. Phys.: Condens. Matter* **2004**, *16*, R481.

(26) Noid, W. Perspective: Coarse-grained Models for Biomolecular Systems. *J. Chem. Phys.* **2013**, *139*, 090901.

(27) Derreumaux, P.; Mousseau, N. Coarse-grained Protein Molecular Dynamics Simulations. *J. Chem. Phys.* **2007**, *126*, 025101.

(28) Tozzini, V. Coarse-grained Models for Proteins. *Curr. Opin. Struct. Biol.* **2005**, *15*, 144–150.

(29) Wang, Y.; Rader, A.; Bahar, I.; Jernigan, R. L. Global Ribosome Motions Revealed with Elastic Network Model. *J. Struct. Biol.* **2004**, *147*, 302–314.

(30) Arkhipov, A.; Freddolino, P. L.; Imada, K.; Namba, K.; Schulten, K. Coarse-grained Molecular Dynamics Simulations of a Rotating Bacterial Flagellum. *Biophys. J.* **2006**, *91*, 4589–4597.

(31) Wheeler, R. A.; Spellmeyer, D. C. *Annual Reports in Computational Chemistry*; Elsevier: Amsterdam, The Netherlands, 2010; Vol. 7.

(32) Gautieri, A.; Russo, A.; Vesentini, S.; Redaelli, A.; Buehler, M. J. Coarse-grained Model of Collagen Molecules Using an Extended MARTINI Force Field. *J. Chem. Theory Comput.* **2010**, *6*, 1210–1218.

(33) Pannuzzo, M.; De Jong, D. H.; Raudino, A.; Marrink, S. J. Simulation of Polyethylene Glycol and Calcium-mediated Membrane Fusion. *J. Chem. Phys.* **2014**, *140*, 124905.

(34) López, C. A.; de Vries, A. H.; Marrink, S. J. Computational Microscopy of Cyclodextrin Mediated Cholesterol Extraction from Lipid Model Membranes. *Sci. Rep.* **2013**, *3*, 2071.

(35) Guo, C.; Luo, Y.; Zhou, R.; Wei, G. Probing the Self-assembly Mechanism of Diphenylalanine-based Peptide Nanovesicles and Nanotubes. *ACS Nano* **2012**, *6*, 3907–3918.

(36) Seo, M.; Rauscher, S.; Pomès, R.; Tieleman, D. P. Improving Internal Peptide Dynamics in the Coarse-grained MARTINI Model: Toward Large-scale Simulations of Amyloid and Elastin-like Peptides. *J. Chem. Theory Comput.* **2012**, *8*, 1774–1785.

(37) Marrink, S. J.; Tieleman, D. P. Perspective on the Martini model. *Chem. Soc. Rev.* **2013**, *42*, 6801–6822.

(38) Hess, B.; Kutzner, C.; Van Der Spoel, D.; Lindahl, E. GROMACS 4: Algorithms for Highly Efficient, Load-balanced, and Scalable Molecular Simulation. *J. Chem. Theory Comput.* **2008**, *4*, 435–447.

(39) Schüttelkopf, A. W.; van Aalten, D. M. F. PRODRG: a Tool for High-throughput Crystallography of Protein-Ligand Complexes. *Acta Crystallogr., Sect. D: Struct. Biol.* **2004**, *D60*, 1355–1363.

(40) Jorgensen, W. L.; Chandrasekhar, J.; Madura, J. D.; Impey, R. W.; Klein, M. L. Comparison of Simple Potential Functions for Simulating Liquid Water. *J. Chem. Phys.* **1983**, *79*, 926–935.

(41) MacKerell, A. D. et al. All-atom Empirical Potential for Molecular Modeling and Dynamics Studies of Proteins. *J. Phys. Chem. B* **1998**, *102*, 3586–3616.

(42) Nosé, S. A Unified Formulation of the Constant Temperature Molecular Dynamics Methods. *J. Chem. Phys.* **1984**, *81*, 511–519.

(43) Parrinello, M.; Rahman, A. Polymorphic Transitions in Single Crystals: A New Molecular Dynamics Method. *J. Appl. Phys.* **1981**, *52*, 7182–7190.

(44) Hockney, R. W.; Eastwood, J. W. *Computer Simulation Using Particles*; CRC Press: Bristol, UK, 2010.

(45) Hess, B.; Bekker, H.; Berendsen, H. J. C.; Fraaije, J. G. E. M. LINCS: a Linear Constraint Solver for Molecular Simulations. *J. Comput. Chem.* **1997**, *18*, 1463–1472.

(46) Essmann, U.; Perera, L.; Berkowitz, M. L.; Darden, T.; Lee, H.; Pedersen, L. G. A Smooth Particle Mesh Ewald Method. *J. Chem. Phys.* **1995**, *103*, 8577–8593.

(47) Allen, M. P.; Tildesley, D. J. *Computer Simulations of Liquids*; Oxford University Press: Oxford, UK, 1989; p 21.

(48) Torrie, G. M.; Valleau, J. P. Nonphysical Sampling Distributions in Monte Carlo Free-energy Estimation: Umbrella Sampling. *J. Comput. Phys.* **1977**, *23*, 187–199.

(49) Kumar, S.; Rosenberg, J. M.; Bouzida, D.; Swendsen, R. H.; Kollman, P. A. The Weighted Histogram Analysis Method for Free-energy Calculations on Biomolecules. I. The Method. *J. Comput. Chem.* **1992**, *13*, 1011–1021.

(50) Periole, X.; Marrink, S.-J. In *Biomolecular Simulations: Methods and Protocols*; Springer: New York City, USA, 2013; pp 533–565.

(51) Marrink, S. J.; Risselada, H. J.; Yefimov, S.; Tieleman, D. P.; De Vries, A. H. The MARTINI Force Field: Coarse Grained Model for Biomolecular Simulations. *J. Phys. Chem. B* **2007**, *111*, 7812–7824.

(52) Sippl, M. J. Calculation of Conformational Ensembles from Potentials of Mean Force: an Approach to the Knowledge-based Prediction of Local Structures in Globular Proteins. *J. Mol. Biol.* **1990**, *213*, 859–883.

(53) Rühle, V.; Junghans, C.; Lukyanov, A.; Kremer, K.; Andrienko, D. Versatile Object-Oriented Toolkit for Coarse-graining Applications. *J. Chem. Theory Comput.* **2009**, *5*, 3211–3223.

(54) *MATLAB, version 9.0 (R2016a)*; The MathWorks Inc.: Natick, Massachusetts, USA, 2016.

(55) Yesylevskyy, S. O.; Schäfer, L. V.; Sengupta, D.; Marrink, S. J. Polarizable Water Model for the Coarse-grained MARTINI Force Field. *PLoS Comput. Biol.* **2010**, *6*, e1000810.

(56) Pall, S.; Abraham, M. J.; Kutzner, C.; Hess, B.; Lindahl, E. In *Solving Software Challenges for Exascale*; Springer International Publishing: Cham, Switzerland, 2014; pp 3–27.

(57) Bussi, G.; Donadio, D.; Parrinello, M. Canonical Sampling through Velocity Rescaling. *J. Chem. Phys.* **2007**, *126*, 014101.

(58) Neumann, R. M. Entropic Approach to Brownian Movement. *Am. J. Phys.* **1980**, *48*, 354–357.

(59) Ardoña, H. A. M.; Tovar, J. D. Energy Transfer Within Responsive pi-Conjugated Coassembled Peptide-based Nanostructures in Aqueous Environments. *Chem. Sci.* **2015**, *6*, 1474–1484.

(60) Fritz, D.; Koschke, K.; Harmandaris, V. A.; van der Vegt, N. F.; Kremer, K. Multiscale Modeling of Soft Matter: Scaling of Dynamics. *Phys. Chem. Chem. Phys.* **2011**, *13*, 10412–10420.

(61) Groot, R. D. Electrostatic Interactions in Dissipative Particle Dynamics–Simulation of Polyelectrolytes and Anionic Surfactants. *J. Chem. Phys.* **2003**, *118*, 11265–11277.

(62) Groot, R. D.; Rabone, K. Mesoscopic Simulation of Cell Membrane Damage, Morphology Change and Rupture by Nonionic Surfactants. *Biophys. J.* **2001**, *81*, 725–736.

(63) Marrink, S. J.; De Vries, A. H.; Mark, A. E. Coarse Grained Model for Semiquantitative Lipid Simulations. *J. Phys. Chem. B* **2004**, *108*, 750–760.

(64) Frenkel, D.; Smit, B. *Understanding Molecular Simulation: From Algorithms to Applications*, 2nd ed.; Elsevier: San Diego, California, USA, 2002.

(65) Wang, J.; Ferguson, A. L. Mesoscale Simulation of Asphaltene Aggregation. *J. Phys. Chem. B* **2016**, *120*, 8016–8035.

(66) Harary, F. *Graph Theory*; Addison-Wesley: Reading, MA, USA, 1969.

(67) Humphrey, W.; Dalke, A.; Schulten, K. VMD – Visual Molecular Dynamics. *J. Mol. Graphics* **1996**, *14*, 33–38.

(68) Grassberger, P.; Procaccia, I. Measuring the Strangeness of Strange Attractors. *Phys. D (Amsterdam, Neth.)* **1983**, *9*, 189–208.

(69) Theiler, J. Efficient Algorithm for Estimating the Correlation Dimension from a Set of Discrete Points. *Phys. Rev. A* **1987**, *36*, 4456.

(70) Theodorou, D. N.; Suter, U. W. Shape of Unperturbed Linear Polymers: Polypropylene. *Macromolecules (Washington, DC, U. S.)* **1985**, *18*, 1206–1214.

(71) Smoluchowski, M. Drei Vortrage uber Diffusion, Brownsche Bewegung und Koagulation von Kolloidteilchen. *Z. Phys.* **1916**, *17*, 557–585.

(72) Leyvraz, F. Scaling Theory and Exactly Solved Models in the Kinetics of Irreversible Aggregation. *Phys. Rep.* **2003**, *383*, 95–212.

(73) Wattis, J. A. An Introduction to Mathematical Models of Coagulation–Fragmentation Processes: a Discrete Deterministic Mean-field Approach. *Phys. D (Amsterdam, Neth.)* **2006**, *222*, 1–20.

(74) Lee, M. H. A Survey of Numerical Solutions to the Coagulation Equation. *J. Phys. A: Math. Gen.* **2001**, *34*, 10219.

(75) Lee, M. H. On the Validity of the Coagulation Equation and the Nature of Runaway Growth. *Icarus* **2000**, *143*, 74–86.

(76) Olivier, B.; Sorensen, C.; Taylor, T. W. Scaling Dynamics of Aerosol Coagulation. *Phys. Rev. A* **1992**, *45*, 5614.

(77) Modler, A. J.; Gast, K.; Lutsch, G.; Damaschun, G. Assembly of Amyloid Protofibrils via Critical Oligomers—a Novel Pathway of Amyloid Formation. *J. Mol. Biol.* **2003**, *325*, 135–148.

(78) Gillam, J.; MacPhee, C. Modelling Amyloid Fibril Formation Kinetics: Mechanisms of Nucleation and Growth. *J. Phys. Condens. Matter* **2013**, *25*, 373101.

(79) Treat, R. P. An Exact Solution of the Discrete Smoluchowski Equation and its Correspondence to the Solution of the Continuous Equation. *J. Phys. A: Math. Gen.* **1990**, *23*, 3003.

(80) Leyvraz, F.; Tschudi, H. Singularities in the Kinetics of Coagulation Processes. *J. Phys. A: Math. Gen.* **1981**, *14*, 3389.

(81) Smoluchowski, M. Versuch Einer Mathematischen Theorie der Koagulationskinetik Kolloider Lösungen. *Pisma Mariana Smoluchowskiego* **1927**, *2*, 595–639.

(82) Lenaz, G. In *Coenzyme Q: Molecular Mechanisms in Health and Disease*; CRC Press: New York City, USA, 2000; Chapter 1, pp 5–28.

(83) Chatterjee, S.; Hadi, A. S. *Regression Analysis by Example*; John Wiley & Sons: Hoboken, NJ, USA, 2015.

(84) Olivier, B.; Sorensen, C. Variable Aggregation Rates in Colloidal Gold: Kernel Homogeneity Dependence on Aggregant Concentration. *Phys. Rev. A* **1990**, *41*, 2093.

(85) Van Dongen, P.; Ernst, M. Dynamic Scaling in the Kinetics of Clustering. *Phys. Rev. Lett.* **1985**, *54*, 1396.

(86) Diegelmann, S. R.; Gorham, J. M.; Tovar, J. D. One-dimensional Optoelectronic Nanostructures Derived from the Aqueous Self-assembly of π-Conjugated Oligopeptides. *J. Am. Chem. Soc.* **2008**, *130*, 13840–13841.

(87) Lees, A.; Edwards, S. The Computer Study of Transport Processes Under Extreme Conditions. *J. Phys. C: Solid State Phys.* **1972**, *5*, 1921.

(88) Kraynik, A.; Reinelt, D. Extensional Motions of Spatially Periodic Lattices. *Int. J. Multiphase Flow* **1992**, *18*, 1045–1059.

(89) Evans, D. J.; Morriss, G. Nonlinear-response Theory for Steady Planar Couette Flow. *Phys. Rev. A* **1984**, *30*, 1528.

(90) Rühle, V.; Lukyanov, A.; May, F.; Schrader, M.; Vehoff, T.; Kirkpatrick, J.; Baumeier, B.; Andrienko, D. Microscopic Simulations of Charge Transport in Disordered Organic Semiconductors. *J. Chem. Theory Comput.* **2011**, *7*, 3335–3345.

(91) Cornil, J.; Beljonne, D.; Calbert, J.-P.; Brédas, J.-L. Interchain Interactions in Organic π-Conjugated Materials: Impact on Electronic Structure, Optical Response, and Charge Transport. *Adv. Mater. (Weinheim, Ger.)* **2001**, *13*, 1053–1067.

(92) Caruso, A.; Siegler, M. A.; Tovar, J. D. Synthesis of Functionalizable Boron-Containing π-Electron Materials that Incorporate Formally Aromatic Fused Borepin Rings. *Angew. Chem.* **2010**, *122*, 4309–4313.
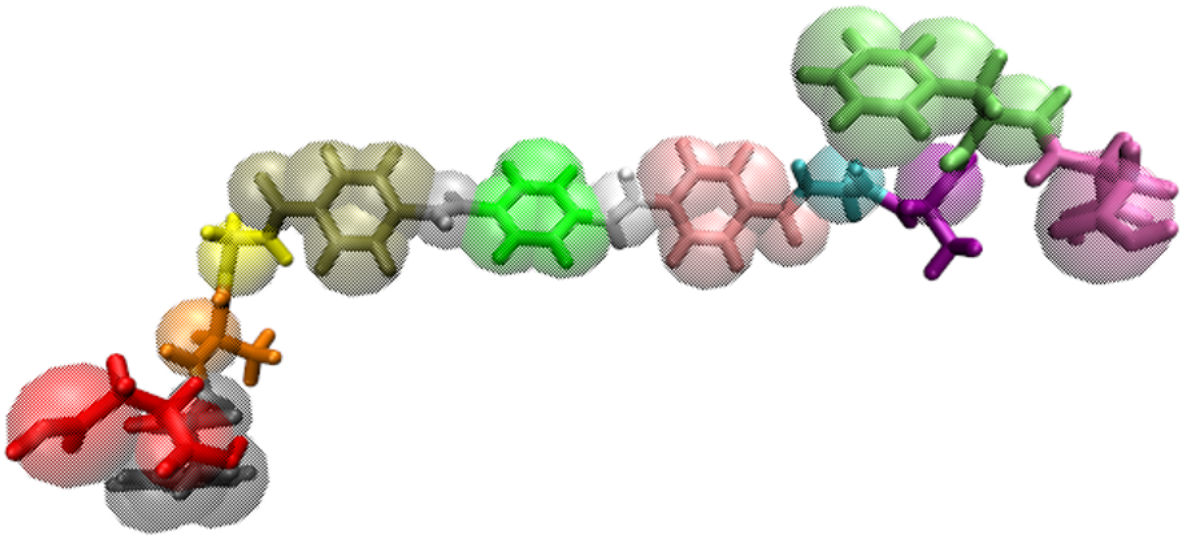
(93) Caruso Jr, A.; Tovar, J. D. Conjugated "B-Entacenes": Polycyclic Aromatics Containing Two Borepin Rings. *Org. Lett.* **2011**, *13*, 3106–3109.